A ^{3}HE-BASED HOLOCENE GLACIAL CHRONOLOGY FROM VILLARRICA VOLCANO, CHILE

By

Yasmeen Esperanza Orellana Salazar

A thesis submitted in partial fulfillment of
the requirements for the degree of

Master of Science

(Geoscience)

at the
UNIVERSITY OF WISCONSIN-MADISON
2024

Date of the final oral examination: October 3rd, 2024

Final Oral Committee:
Shaun Marcott, Associate Professor, Geoscience
Luke Zoet, Associate Professor, Geoscience
Marianne Haseloff, Assistant Professor, Geoscience

Table of Contents

List of Figures

List of Tables

Acknowledgments

I would like to express my deepest gratitude to my advisor, Shaun Marcott, for his invaluable guidance, support, and encouragement throughout my research journey. His expertise and insightful feedback have been instrumental in shaping this thesis.

I thank my committee members, Marianne Haseloff and Luke Zoet, for their constructive critiques and suggestions and for generously sharing their knowledge and time.

I extend my appreciation to my colleagues, fellow students, and professors in the Department of Geoscience at the University of Wisconsin-Madison, whose camaraderie and collaborative spirit have made this experience enriching and enjoyable. Special thanks to M. Tremblay for conducting the measurements and engaging in constructive discussions; P. Moreno-Yaeger for providing me with laboratory work training; E. Mixon for preparing the 2019 samples for measurements; and to M. Romero, J. Klug, C. Volpano, B. Singer, and B. Edwards for their assistance in the field.

This work was funded by the National Science Foundation (NSF) grant EAR-2121570 and the Chilean ANID grant 72220200 Scholarship (Chilean Agency for Research and Development).

Author Contributions

Y. Orellana-Salazar oversaw all aspects of the project, initiated and wrote the manuscript, and prepared samples for measurement. S.A. Marcott designed and conceived the project, oversaw project implementation, performed fieldwork, and co-wrote the manuscript. M.M. Tremblay directed and performed analytical and chemical analyses. P. Moreno-Yaeger prepared samples for analysis. M. Romero performed fieldwork. E.E. Mixon prepared samples for analysis.

A ^{3}He-based Holocene glacial chronology from Villarrica volcano, Chile

Yasmeen Orellana-Salazar[1*], Shaun A. Marcott[1], Marissa M. Tremblay[2], Pablo Moreno-Yaeger[1], Matías Romero[1], Emily E. Mixon[1].

[1]Department of Geoscience, University of Wisconsin-Madison, Madison, Wisconsin, USA
[2]Department of Earth, Atmospheric, and Planetary Sciences, Purdue University, West Lafayette, USA

*Correspondence should be sent to yasmeen.orellanasalazar@wisc.edu

Abstract

Understanding past glacier changes is crucial for deciphering climate variations and predicting the cryosphere's response to future climate shifts. Villarrica volcano is located in the Southern Volcanic Zone (SVZ) and was covered by the Patagonian Ice Sheet (PIS) during the Last Glacial Maximum (LGM) and continues to host glaciers today. Moraines on the flanks of Villarrica demarcate past glacial extents from the latest Pleistocene to the late Holocene, indicating more extensive ice cover than today. However, the post-LGM glacial history on Villarrica and across the SVZ is poorly constrained, limiting our understanding of how glaciers in the Southern Hemisphere behaved during the last deglaciation and Holocene when climate conditions were drastically changing. To constrain the timing of glacial events during the late Holocene, we analyzed olivine-hosted cosmogenic ^{3}He from 25 moraine boulder samples. Our new surface exposure dating chronology reveals several glacial advances occurred during the late Holocene associated with moraine abandonment during the Neoglacial period at 3350 ± 140 a and 1740 ± 225 a, the Little Ice Age (LIA) between 720 ± 340 a and 370 ± 220 a, and modern retreat at 100 ± 50 a. The Neoglacial advances are likely associated with increased Southern Westerly Winds (SWW) and shifts in its position favoring more moisture delivery and glacier growth, while LIA and modern glacial advances are likely due to reduced ablation from decreased temperatures. Our chronology highlights two phases of the latest Holocene glacial retreat in the Southern Hemisphere, which is consistent with both LIA glaciation elsewhere in Patagonia and paleoclimate evidence of delayed industrial-era warming in the Southern Hemisphere beginning around the year 1900.

1. Introduction

The climate plays a crucial role in glacier systems and influences glaciers on global and regional scales. Understanding the significance of climate changes on glaciers is essential for comprehending the complex interaction between Earth's cryosphere and atmospheric systems (Schmittner et al., 2002; Dyurgerov and Meier, 2005). Furthermore, investigating glacier physical changes, whether they are growing or shrinking, under multiple climate scenarios provides visible evidence and a compelling argument for the sensitivity of glacier changes to climate and how accurately it reflects past environmental conditions (Solomina et al., 2016). Investigating past climatic episodes and their impacts on glaciers allows us to comprehend how these natural systems respond to abrupt and centennial-to-millennial scale changes. Patagonia is particularly significant for studying past climatic episodes and their impacts on glaciers due to its vast and dynamic glacial systems, which are highly sensitive to changes in temperature and precipitation. Its unique location in the Southern Hemisphere, influenced by significant climate drivers like the Southern Westerlies and the Southern Ocean (Fletcher and Moreno, 2012; Darvill et al., 2016; Moreno et al., 2018), makes it a key area for understanding global climate patterns. Additionally, Patagonia's well-preserved geological record of glacial activity provides valuable insights into how glaciers have historically responded to abrupt climate shifts, potentially offering a crucial perspective for predicting long-term future trends.

Deglaciation refers to the process of ice sheet and glacier retreat, which has significantly shaped Earth's climate and geography (Alley & Clark, 1999). Termination I refers to the initial phase of rapid deglaciation that marked the end of the Last Glacial Maximum (LGM; ~26 – 19 ka ago) and the transition into the current interglacial period, the Holocene (Clark et al., 2009; Denton et al., 2010). It is characterized by rapid warming, rising sea levels, and significant ice sheet melting (Törnqvist & Hijma, 2012; Lambeck et al., 2014). Although distinct climatic events like the Younger Dryas (YD: 11.6 – 12.9 ka) and the Antarctic Cold Reversal (ACR: 12.9 – 14.5 ka) occurred during the broader deglaciation process, they represent temporary reversals in the overall trend of Termination I (Blunier et al., 1997; Broecker et al., 2010; Putnam et al., 2010; Bromley et al., 2011; Jomelli et al., 2014; Pedro et al., 2016; Sagredo et al., 2018; Cheng et al., 2020). The Holocene interglacial period spans the last 11.7 ka and has been characterized by relatively stable and warm climate conditions compared to the preceding glacial periods (Wanner et al., 2011).

Nevertheless, it also included several centennial and millennial-scale climate oscillations, such as the Holocene Thermal Maximum (10 ka – 6 ka ago), the Medieval Warm Period (800 – 1200 AD), and the Little Ice Age (1300 – 1850 AD) (Hughes & Diaz, 1994; Crowley & Lowery, 2000; Broecker, 2001; Mann, 2002; Wanner et al., 2011; Marcott et al., 2013; PAGES 2k Consortium, 2013). Moreover, these episodes did not affect the climate equally worldwide, and previous research recognizes an abrupt inter-hemispheric, asymmetric climate change generally referred to as the bipolar seesaw (Broecker, 1998; Stocker, 1998; Stocker & Johnsen, 2003; Putnam et al., 2010; Shakun et al., 2012; Pedro et al., 2016; Renssen et al., 2018).

The Patagonia region stretches from the Chilean Lake District (38° – 42°S) in the north to the Cordillera Darwin Icefield in the south. This area includes the southern part of the Patagonian Ice Fields, which are among the largest glacier systems in the Southern Hemisphere (Davies et al., 2020). The Patagonian Ice Fields are divided into several sectors: Northern Patagonian Icefields (NPI; 46° – 48°S); the Southern Patagonian Icefields (SPI; 48°S – 52°S); the Gran Campo Nevado sector (52°S – 53°S); and the Cordillera Darwin sector (53°S – 56°S). Patagonia also comprises the southern section of the Andes Mountains, featuring diverse landscapes on both the Chilean and Argentinian sides. The region is characterized by lakes, fjords, temperate rainforests, and numerous glaciers on the Chilean side. In contrast, the Argentinian side is marked by deserts, tablelands, and steppes.

Modern glacial inventories from the Patagonian Andes south of 45°S come from a total of 11,209 inventoried glaciers as of 2016 (Meier et al., 2018). Most of these glaciers face southeast, although the overall orientation of the mountain ranges influences the larger outlet glaciers. Over the past ~150 years, the glacierized area was reduced from 28,091 ± 890 km^2 to 22,636 ± 905 km^2, resulting in a ~20 ± 5% area loss (Meier et al., 2018). The rate of glacier retreat has accelerated through the years 1870 – 1986, 1986 – 2005, and 2005 – 2016, with annual retreat rates increasing from 0.10 ± 0.04 to 0.33 ± 0.28% and then slightly decreasing to 0.25 ± 0.50%, respectively, particularly affecting smaller glaciers north of the Northern Patagonian Icefield. Over 600 glaciers have entirely disappeared since the Little Ice Age, and more than 650 glaciers have seen an area reduction of over 70% (Masiokas et al., 2020).

The Patagonian Andes host numerous small ice caps and valley glaciers, but today's icefields are remnants of a much larger Patagonian Ice Sheet (PIS) that existed during the LGM around 35 to 18 thousand years ago (Denton et al., 1999). During the LGM, the PIS extended from

38°S to 55°S, comprising terrestrial lobes that retreated into large paleolakes to the east and likely reached the continental shelf on the west coast (Davies et al., 2020). Studying the behavior of the PIS during various climatic conditions and rapid transitions provides valuable insights into the region's response to climate change and its susceptibility to future changes.

The Holocene (11.7 ka – present) climate can be characterized as a warmer climate state than the preceding deglacial and intermittently interrupted by centennial cold periods (Alley et al., 1997; Crowley, 2002; Wanner et al., 2015). Orbital forcing is thought to be the dominant factor influencing glacier fluctuations before significant anthropogenic influence (Solomina et al., 2015). In the Northern Hemisphere (NH), glacier lengths generally increased with decreasing summer insolation, leading to overall glacier growth during the late Holocene (Davis, 1988; Berger and Loutre, 1991; Crowley, 2002; Davis et al., 2009; Solomina et al., 2015, 2016; Zhang et al., 2022). However, in the Southern Hemisphere, high-resolution proxies are limited, and glacier trends do not show the strong correlation between glacier length and summer insolation that is observed in the NH (Wanner et al., 2015). During the late Holocene, as a result of increasing summer insolation, glacier advances, and moraine formations occurred in Southern Patagonia (Clapperton and Sugden, 1988; Glasser et al., 2004; Wanner et al., 2008; Schaefer et al., 2009; Christ et al., 2015). Over the past two millennia, both hemispheres have exhibited coherent glacier advances, often corresponding with periods of high volcanic activity and low solar irradiance (Steinhilber et al., 2009; PAGES 2k Consortium, 2013; Sigl et al., 2015; Solomina et al., 2016). Intervals of sudden ice growth in the NH coincide with two of the most volcanically perturbed half centuries of the past millennium; this resulted in an abrupt summer cooling, which persisted by sea-ice/ocean feedbacks long after volcanic aerosols are dissipated in the NH (Miller et al., 2012).

The LIA marked the coldest temperatures during the Holocene and was the most extensive and geographically widespread event between the 13th and 19th centuries (Mann et al., 1999; Mann, 2002; Matthews & Briffa, 2005; PAGES 2k Consortium, 2013, 2019; Solomina et al., 2016). Although some research has been conducted on the LIA glaciations in the Southern Hemisphere, it has mainly relied on mapping and dating glacier moraines (Villalba, 1994; Schaefer et al., 2009; Davies & Glasser, 2012; Rivera et al., 2012; Putnam et al., 2013; Strelin et al., 2014; Chambers et al., 2014; Turney et al., 2016). There is still very little information about the climate in this hemisphere, which limits our understanding of the spatial fingerprint. However, Southern Patagonia, spanning the western and eastern sides of the Andes, has the longest and most complete record of Quaternary glaciations (Kaplan et al., 2007), offering substantial evidence that glaciers and icefields have expanded and contracted in response to past climate variations (Glasser et al., 2004).

The SVZ (34-46°S) is a unique setting to explore in detail terrestrial glacial events due to the preservation of many glacial features and deposits since the local LGM (Figure 1; Denton et al., 1999; Putnam et al., 2013; Moreno et al., 2015; Davies et al., 2020; Rabassa et al., 2022). Previous efforts to constrain the spatial extent of the Patagonian Ice Sheet have been limited by their focus on individual sub-regions of Patagonia and on the LGM and deglacial glacial deposits (Lowell et al., 1995; Denton et al., 1999; Moreno et al., 2015). To address these limitations and characterize the Holocene glacial extent in the SVZ, we performed surface exposure dating using ^{3}He on boulders obtained along the crests of several moraines on the flanks of Villarrica volcano. Due to its extensive glacial history and well-preserved geomorphological features, the Villarrica volcano in Chile is a prime site for establishing a glacial chronology using surface exposure dating. The volcano's high elevation has allowed for the retention of glacial deposits from multiple past glaciations, while periodic volcanic activity has created tephra layers that serve as valuable chronological markers. The accessibility of Villarrica facilitates thorough field sampling across diverse elevations and the existing body of geological research in the region (Moreno, 2000; Lara and Clavero, 2004; Moreno and Clavero, 2006; Jara et al., 2011) provides a robust framework for interpreting surface exposure dating results within a broader climatic context. Here, we present a new Holocene chronology of the ice retreat from Villarrica volcano, filling critical gaps in the timing of recent glacial changes in northern Patagonia. Our findings enhance the understanding of the regional impacts of global climatic events such as the LIA on the Patagonian Ice Fields, contributing to the broader knowledge of historical climate dynamics and their effects on glacial systems.

2. Geological Background of Villarica Volcano

Villarrica volcano (-39.420147°, -71.939663°; 2847 m a.s.l.) is in the volcanic chain of the Southern Volcanic Zone (SVZ) on the Chilean Andes, and is also known as Rukapillán, from the Mapuche word meaning ''House of the Pillán'' (Pillán: who lives inside volcanoes; Alvarado Pérez & Mera Moreno, 2004). Villarrica volcano is an ice-capped volcano rising above the lake and town of the same name, and it is one of the most active volcanoes in South America, with 59 documented eruptions since 1558 (Lara & Clavero, 2004). Along with the Pleistocene-Holocene Quetrupillán and Lanín stratovolcanoes, they form an NW-SE volcanic chain, which is oblique to the present volcanic arc and a main structure located in the region: the N-S running Liquiñe-Ofqui Fault System (Hickey -Vargas et al., 1989).

Villarrica volcano is capped by three alpine glaciers: Pichillancahue, Voipir and Turbio glaciers. Many authors have grouped the Pichillancahue and Turbio glaciers due to their extension and location, referencing it as the Glaciar Pichillancahue-Turbio, a term adopted here as well (Figure 2). This glacier has been monitored since 2003 (Brock et al., 2007) and digital photography measurements have been carried out since 2005 (Rivera et al., 2008). Glaciar Voipir (Mapuche word that means ‘’new snow’’ in English) has not been monitored, and less is known of its modern changes. Significant volcanic activity has occurred in Villarrica since 1964 (Moreno and Clavero, 2006; Van Daele et al., 2014). Thus, volcanic eruptions in the 1970s and 1980s (1977, 1980, 1983, and 1985) led to substantial glacier area changes, with large volumes of fumarolic and eruptive materials; these eruptions triggered lahars as the volcanic materials melted snow and glacier ice, further contributing to lahar formation as they descended the flanks (Clavero and Moreno, 2004).

Although Villarrica volcano’s historical eruptions have primarily been effusive and weakly explosive, it also has exhibited highly explosive postglacial activity, producing pyroclastic density currents and tephra from both the central vent and flank parasitic pyroclastic cones (Clavero & Moreno, 2004). Despite the diverse eruption styles, Villarrica’s magma has consistently maintained a basaltic to basaltic andesitic composition (50 – 57 wt.% SiO_2), with occasional intra-glacial dacitic domes and pumices (64 wt.% SiO_2) (Moreno & Clavero, 2006). The volcanic products vary texturally from porphyritic (15 – 20% phenocrysts) to less porphyritic flow textures (10% phenocrysts) and are variably vesicular. The basalts and basaltic andesitic rocks are dominated by olivine (Fo_{71-80}), pyroxene (Mg#~50), and plagioclase (An_{60-80}) (Cortés et al., 2024). Notably, olivine and pyroxenes occur as prominent phenocryst phases in most lava flows, often displaying resorbed rims. These minerals' presence and characteristics are particularly important for surface exposure dating with helium, as they influence the retention and diffusion of cosmogenic ^3He, making them crucial for accurate age determinations (Blard, 2021).

2.1. Glacial features around Villarrica volcano

Previous studies have characterized glacial deposits associated with the late Pleistocene cooling in the Villarrica volcano zone (Lara & Clavero, 2004). These deposits consist of lateral and end moraines and glaciofluvial and glaciolacustrine sediments. The moraines, which are remnants from the LGM (Moreno et al., 2015), are situated between ~9 to 17 km away from the modern ice and were formed during the last glacial period as part of the glacial cap of the Villarrica volcano and the larger PIS (Figure 1c). The Licán ignimbrite deposited at 16.8 ka directly overlies the glacial till, suggesting that the PIS had retreated from elevations below 1,000 m a.s.l. some 200 – 500 years earlier (Moreno et al., 2015). Between 11.4 to 5.7 ka, no glacial advances are recorded (Bravo, 2008), which could be related to a lack of deposits or investigations. This phase is generally considered an interval with warmer climatic conditions than the LGM and Younger Dryas (Glasser et al., 2004). However, during the last 5.7 ka, a series of glacial advances have occurred in many mountainous regions of the world, commonly referred to as 'Neoglaciation' (Porter & Denton, 1967). On and adjacent to Villarrica no significant records of Neoglacial advances have been documented, including during the Little Ice Age (LIA). The only evidence of recent Holocene activity consists of small morainic deposits mapped but not dated on the southern and southwestern slopes of the volcano (Clavero & Moreno, 2004).

2.2. Glaciation and climate evolution in Patagonia

Patagonia, situated in the southernmost part of South America, has been a significant region for studying past glaciation and climate change. During the Late Pleistocene, the Patagonian mountain ice cap formed during an initial colder episode (MIS 4, ca. 80-60 ka BP), followed by a warmer interstadial event extending through MIS 3 (ca. 30-60 ka BP). The local LGM, occurring during MIS 2 (ca. 30–15 ka BP), was the coldest episode of the Late Pleistocene, peaking around 24 ka BP (Rabassa et al., 2022). During the LGM, the PIS extensively covered the Andes Mountains from 38 to 55 °S (Davies et al., 2020). Paleoclimate evidence, mostly derived from glacial landforms, suggests significant latitudinal and longitudinal disparities across Patagonia in the timing and magnitude of maximum glaciation during the last glacial cycle. These glacial expansions coincided with a decline in northern hemispheric insolation intensity, atmospheric cooling over Antarctica, and lower sea-surface temperatures in mid-latitude southern ocean basins, supporting the hypothesis of an MIS 2 oceanic and atmospheric cooling signal propagating from the northern to the southern hemisphere (Leger et al., 2021).

The Villarrica volcano (39°S, 71°W) was encased by the PIS and its own local ice cap during the LGM (Figure 1b; Lara & Clavero, 2004) and likely followed the rest of Patagonia and experienced growth and decay throughout previous glacial-interglacial cycles influenced by Earth's orbital change throughout MIS 5-2, which culminated during the LGM (Weber et al., 2012; Peltier et al., 2023). Chronological glacial constraints in this region are based largely on radiocarbon dating of LGM and pre-LGM glacial deposits around lakes such as Llanquihue, Puyehue, Ranco, and Calafquén (Denton et al., 1999; Bertrand et al., 2008; Moreno et al., 2015; García et al., 2021). Cosmogenic nuclide surface exposure dating (^{10}Be and ^{36}Cl) performed on glacier landforms in the southern Chilean Andes (46°S) suggests that glaciers advanced around 8.5 and 6.2 ka, likely driven by a northward migration of the Southern Westerlies, which increased precipitation and/or reduced temperatures at this latitude (Douglass et al., 2005). Additional ^{36}Cl exposure dating on basaltic boulders, alongside dendrochronology and glacier mass balance modeling, has helped to constrain Late Holocene glacial fluctuations at Monte Sierra Nevada (38°S) in the Central-South Chilean Andes, where moraines suggest multiple glacier readvances between 4.2 and 0.8 ka (Price et al., 2022).

Following the LGM, the Antarctic Cold Reversal (ACR), occurring between 14,700 to 12,700 years ago, marked a brief return to colder conditions in the Southern Hemisphere. During this period, Patagonia experienced a resurgence in glacial activity, with glaciers advancing until the climate began to warm (Leger et al., 2021; Rabassa et al., 2022; Castillo-Llarena et al., 2024) and likely only persisting as alpine glaciers in the SVZ (Cuzzone et al., 2023). This glacial behavior is thought to be associated with the northward migration of the westerly wind belt during the ACR, leading to colder temperatures and increased precipitation in the area (García et al., 2012; Moreno et al., 2018).

3. Methodology

3.1. Field sampling

Geomorphic setting and surficial moraine characteristics were carefully considered when selecting moraine boulders for cosmogenic nuclide dating, ensuring they represent glacial processes and provide reliable data (Dunai, 2010; Figure 2). We selected boulders from lateral moraines that were not shielded from cosmic rays by adjacent boulders or vegetation and showed a stable post-depositional history without signs of burial or movement after their initial deposition. We also selected boulders along the tops of the moraine crests, focusing on boulders over 0.3 meters in height to minimize issues related to snow cover, exhumation, and post-depositional movement. The sampling process involved selecting the largest boulders on or near well-defined moraine crests with wide and flat surfaces, avoiding those with evidence of spallation and sharp edges (Table 1). Approximately ~2 kg of material was collected from the upper 2 – 5 cm of the moraine boulders using a hammer and chisel (Figures 3-7). The boulders sampled were basalts and basaltic andesites with more than 5% olivine phenocrysts. The position and elevation of each sample were determined with a handheld GPS. Horizon shielding of the surrounding landscape was measured with a clinometer.

3.2. Mineral separation

Whole rock samples were crushed using a jaw crusher to create a granular material from hand samples. Then, a disk mill was used to grind samples into a range of size fractions from <180 μm to 850 μm. Subsequently, mechanical agitation was applied to a stack of sieves nested together, arranging the sieve with the largest openings at the top to the smallest at the bottom, with a pan underneath to catch anything finer than the smallest sieve. The size fraction selected for our analyses was 250 – 500 μm as the olivine crystals were observed to be the most pristine, intact, and unbroken in this interval. The material was then separated based on magnetic susceptibility, where highly magnetic material was removed using a hand magnet, and weakly magnetic materials were separated by a Frantz magnetic separator using a ramp angle of 15° and strength of the magnetic field of 0.1 A. The resulting separation resulted in a magnetic fraction characterized mainly by groundmass and a non-magnetic fraction composed of olivine, pyroxene, and plagioclase. A magnetic field of 0.4 A was then applied to further isolate the olivines and pyroxenes from the plagioclase fraction. The olivine and pyroxene fractions were then separated based on their density. To achieve this, Methylene Iodide ($\rho = 3.32 \frac{g}{cm^3}$) was utilized to separate the olivine from the pyroxene. The olivine fractions were hand-picked using a Leica Microscope Model MDG41 until ~1 g of olivine crystals with no visible inclusions were obtained.

3.3. ^{3}He measurements and exposure age calculations

Helium isotope measurements were carried out at Berkeley Geochronology Lab for samples VR-19-37, VR-19-39, and VR-19-41, where a MAP-215-50 Single Collector Mass Spectrometer was used. The remaining 22 olivine separates were analyzed in the Noble Gas Spectrometry Laboratory at Purdue University. For all samples, the $^{3}He/^{4}He$ released from the olivine grains was measured during vacuum crushing. The olivine grains were then degassed by heating them with a diode laser. Magmatic $^{3}He/^{4}He$ measured via crushing was used to correct the ^{3}He released by heating in order to obtain the cosmogenic ^{3}He concentration (e.g., Kurz, 1986a, 1986b; Kurz et al., 1990). It is assumed that the samples have negligible radiogenic and nucleogenic helium (e.g., Blard, 2021). This assumption is well-founded, as the source rocks of the moraine boulders sampled date back to the late Holocene. Below, the crushing and heating extraction methods and the methods for cleaning and measuring the extracted gas are described.

3.3.1. Gas extraction by crushing

We loaded an aliquot weighing ~1 g into a vacuum crushing apparatus. This apparatus consists of bellows connected to two modified blank Conflat® flanges. The bottom flange was modified to hold a stainless-steel cup and connect to an extraction line via a branch port. The top flange was modified to accommodate a piston. A sample is loaded into the stainless-steel cup with one or more stainless steel discs stacked on top of the sample and placed under an ultra-high vacuum. A hydraulic cylinder is used to push the top flange and compress the bellows, lowering the internal piston onto the discs and crushing the sample material underneath.

3.3.2. Gas extraction by heating

Following crushing, we weighed and packed the samples into tantalum cups. We packed ~100-250 mg of olivine into each cup and crimped both ends, creating a pillow-shaped packet. The packets were placed under an ultra-high vacuum in a laser microfurnace and heated with a 130 W diode laser. The temperature was controlled via a feedback control loop with an optical pyrometer. The packets were then heated to 1200 ºC for 15 minutes. We also performed a second re-extraction heating step to 1300 ºC for 15 minutes to ensure quantitative helium release. Because the moraines sampled were predicted to be late Holocene in age and, in some cases, as young as the Little Ice Age, we needed to heat multiple tantalum packets of olivine to obtain a measurable amount of cosmogenic ^{3}He. For some samples, we only needed to degas ~0.5 g of olivine and heat 3 packets; for others, we degassed the entire aliquot of olivine that was separated, amounting to > 1 g of olivine and 5-7 packets.

3.3.3. Gas cleanup and measurement

The gas released by crushing or heating was let into an extraction line and cleaned up in two steps: first, by exposure to two SAES GP 50-ST101 getters (one operated at ambient temperature and one operated at ~600 ºC), and then by cryo-focusing using a Janis CCS-TRAP-HT/204 Closed Cycle Cold Trap. Helium was trapped at 13 K, released at 33 K, and then let into an Isotopx NGX noble gas mass spectrometer. The NGX at Purdue is outfitted with a high-sensitivity cathode 'Nier' type gas source and five detectors: two Faraday cups with ATONA® amplifiers and three discrete dynode electron multipliers. Initial measurements demonstrated that the ^{4}He amounts in the olivine separates were small enough that all helium isotope measurements could be carried on an electron multiplier. At the beginning of each measurement, we peak centered using HD (molecular ion of hydrogen and deuterium), which has a constant background intensity in the NGX between 150 and 300 cps. We then measured ^{4}He and ^{3}He signal intensities by peak hopping, with 15 cycles and 15 measurements per cycle for each isotope.

We made blank corrections by measuring both 'hot' blanks by heating empty Ta packets in the same fashion as the samples and 'cold' extraction line blanks with the laser microfurnace and the vacuum crusher. The amounts of ^{4}He and ^{3}He in the hot blanks were indistinguishable from the cold blanks. We determined the mass spectrometer sensitivity by measuring the helium isotopic composition of a monometrically-calibrated gas standard that was created by mixing pure ^{4}He and ^{3}He with a ^{3}He/^{4}He of 0.00238. We can measure four different-sized aliquots of this standard gas: one using the 0.2 cm^{3} pipette volume in front of the standard tank and three by expanding an aliquot in the pipette into two ~3 cm^{3} calibrated safety volumes in front of the pipette. We do not observe a significant dependence of instrument sensitivity on ^{4}He signal intensity (a proxy for pressure, e.g., Burnard and Farley, 2000) over the range of standard aliquots analyzed, and nearly all the crushing and heating measurements had ^{4}He signal intensities within the range of standard intensities.

For several of the crushing measurements, the ^{3}He signal intensities were below the instrument detection limits, preventing us from obtaining a magmatic $^{3}He/^{4}He$ with which to correct the ^{3}He measured during heating. Similarly, other crushing measurements had measurable but low ^{3}He signal intensities, resulting in a magmatic $^{3}He/^{4}He$ with very large uncertainties. However, we also observed that the magmatic $^{3}He/^{4}He$ across virtually all crushing measurements with measurable ^{3}He agreed within uncertainty. We, therefore, opted to use the weighted mean magmatic $^{3}He/^{4}He$ across these measurements to correct the ^{3}He measurements made during heating. This weighted mean $^{3}He/^{4}He$ normalized to the $^{3}He/^{4}He$ of air (known as R/R_a) is 1.96 ± 0.26 (2σ, n = 17).

3.3.4. Cosmogenic ^{3}He calculation

To calculate ^{3}He exposure ages, the ^{3}He concentrations due to cosmogenic production must be determined. After hand-picked olivines have their helium concentrations measured using the Thermochronology Lab protocols, the cosmogenic ^{3}He concentration is determined by subtracting the magmatic component from the total ^{3}He:

$$^{3}He_c = {}^{3}He_t - {}^{3}He_i \quad (1)$$

Where $^{3}He_c$ is cosmogenic, $^{3}He_t$ is released on melting, and $^{3}He_i$ is inherited (magmatic) ^{3}He. $^{3}He_i$ and $^{3}He_t$ are determined as follows:

$$^{3}He_i = {}^{3}He / {}^{4}He_{cr} \times {}^{3}He_m \quad (2)$$

$$^{3}He_t = {}^{3}He / {}^{4}He_m \times {}^{3}He_m \quad (3)$$

Where *cr* denotes values obtained by crushing and *m* denotes values obtained by melting residual powders. Equation 2 assumes that all ^{4}He is magmatic, specifically $^{4}He_i \gg {}^{4}He_c$, and that there are no other ^{4}He components. However, this assumption is only valid for young basalts as older basalts have inherited ^{4}He produced radiogenically during the decay of U and Th, and ^{3}He generated by the thermal neutron capture reaction $^{6}Li\ (n,\alpha)T \rightarrow {}^{3}He$ (Kaplan et al., 2004).

3.3.5. ^{3}He exposure age calculation

The exposure ages were interpreted from the weighted mean of the measurement to estimate precision as the best representation of landform age and were calculated using the online CRONUS-Earth calculator v.3 (Balco et al., 2008; available at: hess.ess.washington.edu/). This calculator requires the sample's latitude, longitude, elevation, thickness, density, shielding, and erosion. To correct the production rate at the sites that are partially shielded from the cosmic ray flux, a topographic shielding correction was made for all the samples using the same website, while the erosion rate was not calculated as it was considered to be negligible. Minimal depth correction was necessary as all samples were collected from the uppermost 5 cm of the rock in which the production of cosmogenic nuclides is constant. The information was then computed using the scaling scheme of Lifton et al. (2014) with a production rate of 119.03 $\pm$ 11.73 at/g/yr (Goehring et al., 2010). External and internal uncertainties are reported at 1σ confidence interval (Hill et al., 1993). Duplicate analyses of ^{3}He concentrations in splits of olivine separated from the same sample were performed for every sample (Table 3), indicating high reproducibility of measurements as overlapped within 1σ analytical uncertainty and all overlap within 2σ.

3.3.6. Factors affecting ^{3}He exposure age determination

We selected ^{3}He as the cosmogenic isotope for this analysis due to its suitability for olivine-rich basaltic and basaltic-andesite samples, which are abundant in the volcanic terrain of Villarrica. While ^{10}Be is commonly used in exposure dating, it requires quartz, a mineral that is absent in mafic volcanic rocks like those in our study area. In contrast, ^{3}He is produced directly within olivine, making it ideal for dating these basaltic to basaltic-andesite surfaces. Additionally, the low diffusion rate of helium in olivine ensures the long-term preservation of ^{3}He, providing accurate and reliable exposure ages.

Thus, using the cosmogenic ^{3}He data allows us to interpret the exposure histories of the samples. We have shown that cosmogenic ^{3}He exposure ages, on the order of <1 ka, can be obtained from samples at mid-to-low-elevation sites (c. 1380 m asl to 1640 m asl) in the mid-latitudes. Resolution of these young ages is aided by (i) the high local production rate of cosmogenic ^{3}He at ~1300 – 1600 m asl elevation of the samples, (ii) at least 1 g of pristine olivine crystals, and (iii) the low concentrations of $^{4}He_{tot}$.

Several factors could explain the low concentrations of background helium in our samples. One possibility is that degassing during crystallization of the small (<500 μm) phenocrysts targeted resulted in low amounts of helium becoming trapped within fluid inclusions. Blard (2021) specifies that observations show that phenocryst size is a first-order control on helium concentrations. However, the fusion of minerals ranging in size from 100 to 500 μm favored reducing the magmatic helium component while avoiding any atmospheric helium contamination.

4. Results

4.1. Cosmogenic ^{3}He concentrations and ages

Helium isotope data from all samples is presented in Table 2. Helium was extracted by melting the olivine phenocrysts from all basaltic andesite samples and the powders that remained after crushing the samples. The ^{3}He/^{4}He of the phenocryst olivine are demonstrably low, ranging from 0.25 to 9.11 R/R$_a$, where R$_a$ is the atmospheric ^{3}He/^{4}He: 1.34×10^{-6}. Total ^{3}He concentrations ranged from 0.16×10^5 atoms to 10.16×10^5 atoms with uncertainties between 0.09×10^5 and 0.41×10^5 atoms (1σ), while total ^{4}He concentrations ranged from 0.70×10^9 atoms to 8.33×10^9 atoms with uncertainties between 0.03×10^9 and 0.94×10^9 atoms (1 σ). Sample CVR-22-37 shows a significantly higher total ^{4}He (42.03×10^9 atoms), likely due to the occurrence of small zircon inclusions. These inclusions, enriched in U and Th, could enhance ^{4}He production through alpha decay, increasing the overall ^{4}He content within the phenocrysts (Blard & Farley, 2008).

Cosmogenic ^{3}He exposure ages from Villarrica volcano lateral moraines are presented in Table 2 and graphically in Figure 8. The oldest moraine is in the southeast and has a bimodal age distribution with mean ages and standard deviations (1σ) of 3350 ± 140 a (n = 3) and 1740 ± 225 a (n = 3) for each distribution. Moraines from the eastern and northwestern flanks are more coherent, with mean ages of 720 ± 340 a (n = 3) and 370 ± 220 a (n = 4), respectively. The youngest moraines are located in the western and southern flanks, with mean ages of 105 ± 55 a (n = 8) and 90 ± 6 a (n = 4), respectively.

5. Discussion

5.1. Moraines age interpretation

Villarrica glacial valleys originate at the terminus of Pichillancahue-Turbio and Voipir glaciers at ~1630 m asl to 1760 m asl on the volcano's upper slopes. A suite of moraine ridges are present 1-3 km down valley from the present glacier terminus. Our field investigation of these landforms, together with the cosmogenic ^{3}He surface exposure ages, supports the idea of late Holocene extension of the ice ~1 km down the valley of Glaciar Voipir and ~3 km down the valley of Glaciar Pichillancahue-Turbio from their present-day termini.

Based on our new ^{3}He chronology, we observe three distinct periods of moraine construction and subsequent abandonment: between 3350 ± 140 a (n = 3) and 1740 ± 225 a (n = 3), between 720 ± 340 a (n = 3) and 370 ± 220 a (n = 4), and between 105 ± 55 a (n = 8) and 90 ± 6 a (n = 4). These intervals represent phases of glacial advance, during which the moraines were constructed, followed by glacial retreat, leading to their abandonment. The oldest moraines on the southeastern flank of the volcano (Figure 6) represent Neoglacial activity (Porter & Denton, 1967), and the middle moraines on the northwestern and eastern flanks (Figure 3 and Figure 7, respectively) represent LIA glaciation (Winkler, 2000; Koch and Kilian, 2005; Harrison et al., 2008; Espizua and Pitte, 2009; Masiokas et al., 2009; Araneda et al., 2009; Rivera et al., 2011, 2012; Aniya and Skvarca, 2012; Malone et al., 2015; González-Reyes et al., 2019; Carrivick et al., 2020; Marta et al., 2021; Simms et al., 2021). The youngest moraines on the western and southern flanks (Figure 4 and Figure 5, respectively) are modern glacial deposits likely related to retreat during pre-industrial warming (Russell et al., 2006; Abram et al., 2016; PAGES2k Consortium et al., 2017; Golledge et al., 2019; PAGES 2k Consortium, 2019; Roe et al., 2021; Deng et al., 2022; Bosson et al., 2023). Various locations across Patagonia also demonstrate multiple mid to late Holocene glacial advances (Figure 9d) and demonstrate common Patagonia-wide Holocene glacial advances (Douglass et al., 2005; Kaplan et al., 2007, 2016; Harrison et al., 2008; Strelin et al., 2014; Sagredo et al., 2016; Nimick et al., 2016; Hein et al., 2017; Reynhout et al., 2019; Price et al., 2022).

We found moraine ages corresponding to the Neoglacial, LIA, and modern glaciation on different volcano flanks. However, it was not possible to identify multiple distinct glacial ages on the same flank. This is likely due to the high volcanic activity of Villarrica volcano, where frequent lava flows and lahars randomly reworked or buried glacial deposits. This process is not selective to moraines of any particular age but occurs unpredictably, affecting the preservation of different glacial phases across the volcano.

5.1.1. Late Holocene glaciation and volcanism

Our Neoglacial moraines come from the southeastern flanks of Villarrica, which are ~2.6 km from the modern ice. The moraines exhibit a clear bimodal age distribution, possibly suggesting two distinct Neoglacial moraine-building phases (Table 2). We hypothesize that the bimodal distribution is related to the geometry of the glacial valley (Figure 6) and the impounding of the ice by large preexisting lava flows of the Early Holocene age (Moreno-Yaeger et al., unpublished). Because glaciers tend to rework or bury existing moraines in the landscape (Porter et al., 2019), our bimodal moraine boulder age distribution is somewhat unusual and difficult to interpret easily. However, the strong grouping of the ages and the field evidence lends us to think that as glaciers advanced and filled the valleys, the ice thickness was nearly equivalent to the height of the lava flows onto which the moraine is deposited and did not fully override the lava flow (Figure 6). The moraines, less than 5 meters thick, likely formed through the deposition of thin supraglacial debris during two glacial phases without being significantly reworked or overridden by subsequent advances.

This bimodal pattern is unlikely to be attributable to analytical uncertainties, inheritance, snow cover distribution, or differential erosion; the ages within each distribution are relatively consistent, and the distribution of the moraine boulders ages across the feature appears to be mixed (Figure 8). We would expect if inheritance was present for it to be randomly distributed throughout our dataset (n=6) and for erosion and snow cover to be consistent amongst the boulders since boulder heights and lithologies were similar (Figure 6). Moreover, the youngest moraines, with their shorter exposure durations, are particularly valuable for assessing the potential influence of inheritance and demonstrate no significance (i.e., >100s years) inherited isotopes from a relatively large population (n=12). We interpret the bimodal distribution as representing two separate glacial advances that deposited boulders in overlapping areas around preexisting lava flows. We interpret the second advance as adding new boulders onto the moraine surface without significantly reworking the existing moraine.

5.1.2. LIA glaciation and local volcanism

The LIA moraines are preserved both on the northwestern and eastern flanks of the volcano and extend to ~1-1.5 km from the modern glaciers and between 1390 m asl and 1640 m asl elevation (Figure 3; Figure 7). The LIA moraine ages are 720 ± 340 a (n = 3) and 370 ± 220 a (n = 4), which are separated by ~350 years. We interpret the age range for the LIA moraines as likely representing two distinct phases of glaciation within the LIA. Notably, glacial and volcanic environments can erase deposition records of prior activity through younger advances and eruptions, making deciphering glacial histories in active volcanic terrains particularly difficult (Scott, 1977; Marcott et al., 2009). Villarrica has been one of the most active Holocene volcanoes in South America, with multiple late Holocene vents and lava flow along its flanks (Muñoz, 1983; Gurioli et al., 2008; Van Daele et al., 2014; Moreno-Yaeger et al., unpublished). Therefore, we expect that many of the prior existing glacial features in each valley have been reworked by Holocene lava flows and lahars, and we infer that other deposits related to these two LIA advances may not be preserved in each valley.

Insights into the interaction between volcanic activity and glacial dynamics can be inferred from exposure ages here and in Moreno-Yaeger et al. (unpublished). It is interpreted that the northwestern glacier advanced soon after a Late Holocene lava flow was deposited, suggesting that it did not impede glacier flow for an extended period (Figure 3). Instead, the lava flow underlies the LIA moraine, given that it has a mean age and standard deviation of 2.5 ± 0.3 ka (1σ) (Moreno-Yaeger et al., unpublished). Our eastern glacier moraine abandonment occurred before the prehistoric lava flow that now fills the valley downhill of the moraines (Figure 7). These findings contribute to a broader understanding of Villarrica's volcanic and glacial history, helping to frame the timeline of past volcanic activity and its influence on glacial dynamics where preservation allows.

5.1.3. Modern glaciation and volcanism

The modern glacial moraines are preserved on both the western and southern flanks of the volcano, extending to ~1-1.5 km from the modern glaciers at elevations between 1500 m asl and 1590 m asl (Figure 4; Figure 5). The exposure ages for these modern moraines are 105 ± 55 a (n = 8) and 90 ± 6 a (n = 4) and overlap within uncertainties. Given the close similarity in ages, we combined them into a single age of 100 ± 50 a. These moraines are the youngest features in our study, having been exposed only within the past century and marking the extent of modern glaciation prior to industrial-era warming (Abram et al. 2016). Despite having more dates from these moraines compared to the other sites, we do not attribute this to better Villarrica-wide preservation, as the moraines are only observed on the western and southern flanks of the volcano. Van Daele et al. (2014) reported 112 eruptions over the last ~600 yr for Villarrica volcano, with at least 22 of those events generating lahars. Petit-Breuilh Sepúlveda (2006) estimated ~50 eruptions in the last ~300 yr. These frequent eruptive events likely affected most of the volcano's flanks, reworking or burying glacial deposits. It is plausible that the absence of moraines on other flanks is due to this volcanic activity rather than differing glacial behavior across the volcano (Thouret et al., 2007; Eaves and Brook, 2021).

Modern glacial variations at Villarrica volcano were analyzed using a combination of aerial photographs and satellite imagery. Lara and Clavero (2004) mapped glaciers around the volcano during multiple years -1945, 1961, 1983, 1987, 1998, and 2003- revealing changes in glacial extent. Notably, glaciers from 1945 appear to have filled the valley adjacent to our eastern LIA moraines (Figure 7), indicating that they have significantly thinned since the LIA. Thus observation correlates with findings from Rivera et al. (2006), who determined a thinning rate of 0.81 ± 0.45 myr^{-1} for Glaciar Pichillancahue-Turbio between 1961 and 2004, along with an area loss of 13% recorded between 1979 and 2005. By 1961, the glaciers across Villarrica had retreated but remained within 500 meters of our modern moraines. Historical imagery from 1985, captured by Landsat and Copernicus and available through Google Earth Pro, reveals that the glacier was still around 500 meters from both the western and southern flanks of the volcano, similar to analysis of glacier position done from 1986 imagery (Reinthaler et al. (2019).

5.2. Late Holocene glaciation in the SVZ and paleoclimatic significance

The PIS in the SVZ has experienced periods of both minor to moderate fluctuations in ice mass with episodes of loss and gain (Hagemann et al., 2024). By 15 ka, there is no evidence of a large and connected PIS with ice that only exists in the highest mountain terrains as alpine glaciers (Cuzzone et al., 2023). Following the large-scale ice retreat, the ACR initiated some glacial advances across Patagonia (Moreno et al., 2009; García et al., 2012; Davies et al., 2018; Mendelová et al., 2020) before they again retreated due to temperatures continuing to rise into the early Holocene (Kilian & Lamy, 2012; Kaplan et al., 2016). A few well-dated moraines across

Patagonia constrain stillstands or readvances during the middle to late Holocene at ca 5 ka and 2 – 1 ka, slightly larger than the 0.5 – 0.2 ka glacial advance (Davies et al., 2020).

Several studies have reconstructed the SWW positions during the Holocene, primarily based on precipitation proxies and their correlation to wind changes (Lamy et al., 2010, 2015; Knudson et al., 2011; Kilian & Lamy, 2012; Voigt et al., 2015; Riechelson et al., 2023). During the late Holocene, the influence of the SWW on the regional climate and glacier dynamics in Patagonia evolved. Reduced SWW strength in Patagonia between ~9.3-7.2 ka resulted in drier conditions and limited glaciation (Flores-Aqueveque et al. (2024); between ~7.2 and 5 ka, the SWW strengthened, leading to cooler, wetter conditions and increased glacial activity. This influence further intensified between ~5 and 0 ka, peaking between ~2.2-0.5 ka, when glaciers experienced their most significant advances due to strong SWW. A subsequent decline in SWW strength between ~0.5 and 0 ka contributed to warmer, drier conditions and glacier retreat. This pattern suggests that the formation of our Neoglacial moraines may have been driven by short-term increases in precipitation linked to stronger SWW. In contrast, our LIA and modern moraines correlate with periods of relatively high precipitation associated with strong SSW, though with less intense SWW influence compared to the Neoglacial period. Changes in regional climate patterns, such as shifts in atmospheric circulation and the SWW positioning, could have impacted these glacial conditions by altering wind patterns, increasing moisture delivery to the region, and influencing glacier mass balance (Kilian & Lamy, 2012). Low insolation is associated with weakened and/or northward displaced SWW and more frequent El Niño events (Fletcher & Moreno, 2012; Kilian & Lamy, 2012; Flores-Aqueveque et al., 2024), resulting in less cold-water upwelling and warm-water masses remaining closer to the western coast of South America, which disrupted global weather patterns. Nevertheless, Varma et al. (2011, 2012) suggested that over the past 3 ka, the SWW changes in central Chile have been influenced by periods of lower solar activity, causing equatorward shifts of the annual mean SWW and vice versa. Moy et al. (2008) identified that the last millennium was dominated by intense westerly flow, increased precipitation, and highly evaporative conditions. When combined with Antarctic ice core data, they indicated that these changes were regional rather than local and that the intensification of the westerlies during the LIA was accompanied by a poleward shift in the southern margin of the wind field, resulting in increased winter precipitation and cooler summer temperatures, which contributed to glacier advances during this period.

Tree-ring and modeling-based temperature reconstructions agree for the late Holocene, with estimates about 1 – 2°C colder than present between ~600 and ~200 years ago, with the lowest temperatures earlier in this interval (Kaplan et al., 2016). Others have also noted that glaciers in the middle latitudes of South America advanced during the last ~600 years (Figure 9; Harrison et al., 2008; Strelin et al., 2014; Kaplan et al., 2016; Reynhout et al., 2019; Price et al., 2022). However, these investigations reveal that the glacial advances were less expansive than those during the mid-Holocene. Consequently, only our LIA advances are likely controlled by reduced ablation through lowered temperatures (Kilian & Lamy, 2012), while our Neoglacial advances were more likely driven by short-term increases in the strength of the SWW and changes in insolation patterns, which contributed to a northward displacement of the SWW (Fletcher & Moreno, 2012).

We compare our new chronology to temperature and glacial records from Patagonia (Figure 9). The glacial advances observed in our ^{3}He ages reveal that our Neoglacial advances do not align well with other glacial records from northern Patagonia. However, our LIA advances appear to represent a widespread glaciation, aligning well with other records across the area and coinciding with a Southern Hemisphere-wide cooling event (Luckman, 2000; Mann et al., 2009; Chambers et al., 2014; Li et al., 2016; Kaplan et al., 2016; Rowan, 2017; Dong et al., 2017; Frugone-Álvarez et al., 2020; Wanner et al., 2022). In contrast, our modern advances are linked to pre-industrial warming, which occurred ~50 – 100 years later than the Northern Hemisphere deglaciation following the LIA (Abram et al., 2016). Insolation in the Southern Hemisphere in the late Holocene is high compared to the NH (Laskar et al., 2004).While higher insolation is typically associated with warmer conditions, our ^{3}He ages suggest glaciers were stable during these times, indicating that factors beyond temperature, such as increased precipitation, may have played a crucial role in influencing glacial dynamics. This pattern is consistent with regional, mid-latitude climate processes, which are likely driven by a combination of temperature and precipitation variability. While insolation changes may influence long-term climate trends, our results underscore the primary role of temperature in driving the glacial advances in Patagonia, especially during the LIA. Additionally, these findings offer new insights into how regional climate patterns, rather than simply global mechanisms like the bipolar seesaw (Broecker, 1998), may explain some of the differences observed between interhemispheric climate records (Vandergoes et al., 2005).

6. Conclusion

We used ^{3}He surface exposure dating from 25 samples collected from boulder moraines around Villarrica volcano in the SVZ to provide a comprehensive chronology of glacial advances during the late Holocene. The ^{3}He exposure ages suggest that the glaciers at Villarrica volcano reached local maxima during two distinct Neoglacial phases at 3350 ± 140 a and 1740 ± 225 a, driven by increased precipitation linked to strengthening SWW and shifts toward the SVZ (Kilian & Lamy, 2012; Moreno et al., 2018). Additionally, glacial advances at 720 ± 340 a and 370 ± 220 a occurred during the LIA, a period characterized by cooler temperatures (Meyer & Wagner, 2009), with continued advances until ~100 ± 50 a, coinciding with the onset of pre-industrial warming (Abram et al., 2016). These findings enhance our understanding of late Holocene glaciation in the region, demonstrating that the glaciers of Villarrica volcano responded to both global cooling and regional precipitation increases.

The glacial advances observed in both hemispheres during the late Holocene highlight the global significance of these climate events despite some regional asynchrony in timing and extent. Specifically, our regional offset suggests that while Patagonia Ice Fields generally responded to global climate drivers, local environmental factors such as regional precipitation patterns and volcanic activity played a crucial role in shaping glacial behavior. Future research should focus on expanding glacial chronologies to better understand the interplay between global climate forcings and local dynamics in Patagonia.

References

Abram, N.J., McGregor, H.V., Tierney, J.E., Evans, M.N., McKay, N.P., and Kaufman, D.S., 2016, Early onset of industrial-era warming across the oceans and continents: Nature, v. 536, p. 411–418, doi:10.1038/nature19082.

Alley, R.B., and Clark, P.U., 1999, The deglaciation of the Northern Hemisphere: A Global Perspective: Annual Review of Earth and Planetary Sciences, v. 27, p. 149–182, doi:10.1146/annurev.earth.27.1.149.

Alley, R.B., Mayewski, P.A., Sowers, T., Stuiver, M., Taylor, K.C., and Clark, P.U., 1997, Holocene climatic instability: A prominent, widespread event 8200 yr ago: Geology, v. 25, p. 483, doi:10.1130/0091-7613(1997)025<0483:HCIAPW>2.3.CO;2.

Alvarado Pérez, M., and Mera Moreno, R., 2004, Estética del paisaje y reconstrucción arqueológica: El caso de la Región del Calafquén (IX y X Región-Chile): Chungará (Arica), v. 36, doi:10.4067/S0717-73562004000400004.

Aniya, M., and Skvarca, P., 2012, Little Ice Age advances of Glaciar Perito Moreno, Hielo Patagónico Sur, South America: Bulletin of Glaciological Research, v. 30, p. 1–8, doi:10.5331/bgr.30.1.

Araneda, A., Torrejón, F., Aguayo, M., Alvial, I., Mendoza, C., and Urrutia, R., 2009, Historical records of Cipreses glacier (34°S): combining documentary-inferred 'Little Ice Age' evidence from Southern and Central Chile: The Holocene, v. 19, p. 1173–1183, doi:10.1177/0959683609345079.

Balco, G., Stone, J.O., Lifton, N.A., and Dunai, T.J., 2008, A complete and easily accessible means of calculating surface exposure ages or erosion rates from 10Be and 26Al measurements: Quaternary Geochronology, v. 3, p. 174–195, doi:10.1016/j.quageo.2007.12.001.

Beck, J., Bock, M., Schmitt, J., Seth, B., Blunier, T., and Fischer, H., 2018, Bipolar carbon and hydrogen isotope constraints on the Holocene methane budget: Biogeosciences, v. 15, p. 7155–7175, doi:10.5194/bg-15-7155-2018.

Bereiter, B., Eggleston, S., Schmitt, J., Nehrbass-Ahles, C., Stocker, T.F., Fischer, H., Kipfstuhl, S., and Chappellaz, J., 2015, Revision of the EPICA Dome C CO_2 record from 800 to 600 kyr before present: Geophysical Research Letters, v. 42, p. 542–549, doi:10.1002/2014GL061957.

Berger, A., and Loutre, M.F., 1991, Insolation values for the climate of the last 10 million years: Quaternary Science Reviews, v. 10, p. 297–317, doi:10.1016/0277-3791(91)90033-Q.

Bertrand, S., Charlet, F., Charlier, B., Renson, V., and Fagel, N., 2008, Climate variability of southern Chile since the Last Glacial Maximum: a continuous sedimentological record from Lago Puyehue (40°S): Journal of Paleolimnology, v. 39, p. 179–195, doi:10.1007/s10933-007-9117-y.

Blard, P.-H., 2021, Cosmogenic 3He in terrestrial rocks: A review: Chemical Geology, v. 586, p. 120543, doi:10.1016/j.chemgeo.2021.120543.

Blard, P.-H., and Farley, K.A., 2008, The influence of radiogenic 4He on cosmogenic 3He determinations in volcanic olivine and pyroxene: Earth and Planetary Science Letters, v. 276, p. 20–29, doi:10.1016/j.epsl.2008.09.003.

Blunier, T., Schwander, J., Stauffer, B., Stocker, T., Dällenbach, A., Indermühle, A., Tschumi, J., Chappellaz, J., Raynaud, D., and Barnola, J. -M., 1997, Timing of the Antarctic cold reversal and the atmospheric CO_2 increase with respect to the Younger Dryas Event: Geophysical Research Letters, v. 24, p. 2683–2686, doi:10.1029/97GL02658.

Bosson, J.B., Huss, M., Cauvy-Fraunié, S., Clément, J.C., Costes, G., Fischer, M., Poulenard, J., and Arthaud, F., 2023, Future emergence of new ecosystems caused by glacial retreat: Nature, v. 620, p. 562–569, doi:10.1038/s41586-023-06302-2.

Bravo, C., 2008, Reconstrucción de Sistemas Glaciares en el Volcán Villarrica, Región de Los Lagos, Chile [Memoria para optar al Título de Geógrafo]: Universidad de Chile.

Brock, B., Rivera, A., Casassa, G., Bown, F., and Acuña, C., 2007, The surface energy balance of an active ice-covered volcano: Villarrica Volcano, southern Chile: Annals of Glaciology, v. 45, p. 104–114, doi:10.3189/172756407782282372.

Broecker, W.S., 1998, Paleocean circulation during the Last Deglaciation: A bipolar seesaw? Paleoceanography, v. 13, p. 119–121, doi:10.1029/97PA03707.

Broecker, W.S., 2001, Was the Medieval Warm Period Global? Science, v. 291, p. 1497–1499, doi:10.1126/science.291.5508.1497.

Broecker, W.S., Denton, G.H., Edwards, R.L., Cheng, H., Alley, R.B., and Putnam, A.E., 2010, Putting the Younger Dryas cold event into context: Quaternary Science Reviews, v. 29, p. 1078–1081, doi:10.1016/j.quascirev.2010.02.019.

Bromley, G.R.M., Hall, B.L., Schaefer, J.M., Winckler, G., Todd, C.E., and Rademaker, K.M., 2011, Glacier fluctuations in the southern Peruvian Andes during the late-glacial period, constrained with cosmogenic ^{3}He: Journal of Quaternary Science, v. 26, p. 37–43, doi:10.1002/jqs.1424.

Burnard, P.G., and Farley, K.A., 2000, Calibration of pressure-dependent sensitivity and discrimination in Nier-type noble gas ion sources: Geochemistry, Geophysics, Geosystems, v. 1, p. 2000GC000038, doi:10.1029/2000GC000038.

Carrivick, J.L., James, W.H.M., Grimes, M., Sutherland, J.L., and Lorrey, A.M., 2020, Ice thickness and volume changes across the Southern Alps, New Zealand, from the little ice age to present: Scientific Reports, v. 10, p. 13392, doi:10.1038/s41598-020-70276-8.

Castillo-Llarena, A., Retamal-Ramírez, F., Bernales, J., Jacques-Coper, M., Prange, M., and Rogozhina, I., 2024, Climate and ice sheet dynamics in Patagonia throughout marine isotope stages 2 and 3: Climate of the Past, v. 20, p. 1559–1577, doi:10.5194/cp-20-1559-2024.

Chambers, F.M., Brain, S.A., Mauquoy, D., McCarroll, J., and Daley, T., 2014, The 'Little Ice Age' in the Southern Hemisphere in the context of the last 3000 years: Peat-based proxy-climate data from Tierra del Fuego: The Holocene, v. 24, p. 1649–1656, doi:10.1177/0959683614551232.

Cheng, H. et al., 2020, Timing and structure of the Younger Dryas event and its underlying climate dynamics: Proceedings of the National Academy of Sciences, v. 117, p. 23408–23417, doi:10.1073/pnas.2007869117.

Christ, A.J. et al., 2015, Late Holocene glacial advance and ice shelf growth in Barilari Bay, Graham Land, west Antarctic Peninsula: Geological Society of America Bulletin, v. 127, p. 297–315, doi:10.1130/B31035.1.

Clapperton, C., and Sugden, D., 1988, Holocene glacier fluctuations in South America and Antarctica: Quaternary Science Reviews, v. 7, p. 185–198, doi:10.1016/0277-3791(88)90005-4.

Clark, P.U., Dyke, A.S., Shakun, J.D., Carlson, A.E., Clark, J., Wohlfarth, B., Mitrovica, J.X., Hostetler, S.W., and McCabe, A.M., 2009, The Last Glacial Maximum: Science, v. 325, p. 710–714, doi:10.1126/science.1172873.

Clavero, J., and Moreno, H., 2004, Evolution of Villarrica volcano, *in* Boletín de Servicio Nacional de Geología y Minería, Gobierno de Chile, v. 61, p. 17–27.

Cortés, J.A., Gertisser, R., and Calder, E.S., 2024, Magma recharge in persistently active basaltic–andesite systems and its geohazards implications: the case of Villarrica volcano, Chile: International Journal of Earth Sciences, doi:10.1007/s00531-024-02414-w.

Crowley, T.J., 2002, Cycles, Cycles Everywhere: Science, v. 295, p. 1473–1474, doi:10.1126/science.1069617.

Crowley, T.J., and Lowery, T.S., 2000, How Warm Was the Medieval Warm Period? AMBIO: A Journal of the Human Environment, v. 29, p. 51–54, doi:10.1579/0044-7447-29.1.51.

Cuzzone, J., Romero, M., and Marcott, S., 2023, Modeling the timing of Patagonian Ice Sheet retreat in the Chilean Lake District from 23–10 ka: Ice sheets/Numerical Modelling preprint, doi:10.5194/tc-2023-68.

Darvill, C.M., Bentley, M.J., Stokes, C.R., and Shulmeister, J., 2016, The timing and cause of glacial advances in the southern mid-latitudes during the last glacial cycle based on a synthesis of exposure ages from Patagonia and New Zealand: Quaternary Science Reviews, v. 149, p. 200–214, doi:10.1016/j.quascirev.2016.07.024.

Davies, B.J. et al., 2020, The evolution of the Patagonian Ice Sheet from 35 ka to the present day (PATICE): Earth-Science Reviews, v. 204, p. 103152, doi:10.1016/j.earscirev.2020.103152.

Davies, B.J., and Glasser, N.F., 2012, Accelerating shrinkage of Patagonian glaciers from the Little Ice Age (~AD 1870) to 2011: Journal of Glaciology, v. 58, p. 1063–1084, doi:10.3189/2012JoG12J026.

Davies, B.J., Thorndycraft, V.R., Fabel, D., and Martin, J.R.V., 2018, Asynchronous glacier dynamics during the Antarctic Cold Reversal in central Patagonia: Quaternary Science Reviews, v. 200, p. 287–312, doi:10.1016/j.quascirev.2018.09.025.

Davis, P., 1988, Holocene glacier fluctuations in the American Cordillera: Quaternary Science Reviews, v. 7, p. 129–157, doi:10.1016/0277-3791(88)90003-0.

Davis, P.T., Menounos, B., and Osborn, G., 2009, Holocene and latest Pleistocene alpine glacier fluctuations: a global perspective: Quaternary Science Reviews, v. 28, p. 2021–2033, doi:10.1016/j.quascirev.2009.05.020.

Deng, K., Azorin-Molina, C., Yang, S., Hu, C., Zhang, G., Minola, L., and Chen, D., 2022, Changes of Southern Hemisphere westerlies in the future warming climate: Atmospheric Research, v. 270, p. 106040, doi:10.1016/j.atmosres.2022.106040.

Denton, G.H., Anderson, R.F., Toggweiler, J.R., Edwards, R.L., Schaefer, J.M., and Putnam, A.E., 2010, The Last Glacial Termination: Science, v. 328, p. 1652–1656, doi:10.1126/science.1184119.

Denton, G.H., Lowell, T.V., Heusser, C.J., Schluchter, C., Andersen, B.G., Heusser, L.E., Moreno, P.I., and Marchant, D.R., 1999, Geomorphology, Stratigraphy, and Radiocarbon Chronology of LlanquihueDrift in the Area of the Southern Lake District, Seno Reloncavi, and Isla Grande de Chiloe, Chile: Geografiska Annaler, Series A: Physical Geography, v. 81, p. 167–229, doi:10.1111/j.0435-3676.1999.00057.x.

Dong, G., Zhou, W., Yi, C., Zhang, L., Li, M., Fu, Y., and Zhang, Q., 2017, Cosmogenic ^{10}Be surface exposure dating of 'Little Ice Age' glacial events in the Mount Jaggang area, central Tibet: The Holocene, v. 27, p. 1516–1525, doi:10.1177/0959683617693895.

Douglass, D.C., Singer, B.S., Kaplan, M.R., Ackert, R.P., Mickelson, D.M., and Caffee, M.W., 2005, Evidence of early Holocene glacial advances in southern South America from cosmogenic surface-exposure dating: Geology, v. 33, p. 237, doi:10.1130/G21144.1.

Dunai, T.J., 2010, Cosmogenic nuclides: principles, concepts and applications in the earth surface sciences.: Cambridge University Press.

Dyurgerov, M., and Meier, M.F., 2005, Glaciers and the changing Earth system: a 2004 snapshot: v. 58.

Eaves, S.R., and Brook, M.S., 2021, Glaciers and glaciation of North Island, New Zealand: New Zealand Journal of Geology and Geophysics, v. 64, p. 1–20, doi:10.1080/00288306.2020.1811354.

Espizua, L.E., and Pitte, P., 2009, The Little Ice Age glacier advance in the Central Andes (35°S), Argentina: Palaeogeography, Palaeoclimatology, Palaeoecology, v. 281, p. 345–350, doi:10.1016/j.palaeo.2008.10.032.

Fletcher, M.-S., and Moreno, P.I., 2012, Have the Southern Westerlies changed in a zonally symmetric manner over the last 14,000 years? A hemisphere-wide take on a controversial problem: Quaternary International, v. 253, p. 32–46, doi:10.1016/j.quaint.2011.04.042.

Flores-Aqueveque, V., Villaseñor, T., Gómez-Fontealba, C., Alloway, B.V., Alfaro, S., Pizarro, H., Guerra, L., and Moreno, P.I., 2024, Multisequal aeolian deposition during the Holocene in southwestern Patagonia (51°S) was modulated by southern westerly wind intensity and vegetation type: Quaternary Science Reviews, v. 331, p. 108616, doi:10.1016/j.quascirev.2024.108616.

Frugone-Álvarez, M. et al., 2020, Volcanism and climate change as drivers in Holocene depositional dynamic of Laguna del Maule (Andes of central Chile – 36° S): Climate of the Past, v. 16, p. 1097–1125, doi:10.5194/cp-16-1097-2020.

García, J.L., Kaplan, M.R., Hall, B.L., Schaefer, J.M., Vega, R.M., Schwartz, R., and Finkel, R., 2012, Glacier expansion in southern Patagonia throughout the Antarctic cold reversal: Geology, v. 40, p. 859–862, doi:10.1130/G33164.1.

García, J.-L., Lüthgens, C., Vega, R.M., Rodés, Á., Hein, A.S., and Binnie, S.A., 2021, A composite 10Be, IR-50 and 14C chronology of the pre-Last Glacial Maximum (LGM) full ice extent of the western Patagonian Ice Sheet on the Isla de Chiloé, south Chile (42° S): E&G Quaternary Science Journal, v. 70, p. 105–128, doi:10.5194/egqsj-70-105-2021.

Glasser, N.F., Harrison, S., Winchester, V., and Aniya, M., 2004, Late Pleistocene and Holocene palaeoclimate and glacier fluctuations in Patagonia: Global and Planetary Change, v. 43, p. 79–101, doi:10.1016/j.gloplacha.2004.03.002.

Goehring, B.M., Kurz, M.D., Balco, G., Schaefer, J.M., Licciardi, J., and Lifton, N., 2010, A reevaluation of in situ cosmogenic 3He production rates: Quaternary Geochronology, v. 5, p. 410–418, doi:10.1016/j.quageo.2010.03.001.

Golledge, N.R., Keller, E.D., Gomez, N., Naughten, K.A., Bernales, J., Trusel, L.D., and Edwards, T.L., 2019, Global environmental consequences of twenty-first-century ice-sheet melt: Nature, v. 566, p. 65–72, doi:10.1038/s41586-019-0889-9.

González-Reyes, Á., Bravo, C., Vuille, M., Jacques-Coper, M., Rojas, M., Sagredo, E., and McPhee, J., 2019, Glacier equilibrium line altitude variations during the "Little Ice Age" in the Mediterranean Andes (30◦–37◦ S):, doi:10.5194/cp-2019-37.

Gurioli, L., Harris, A.J.L., Houghton, B.F., Polacci, M., and Ripepe, M., 2008, Textural and geophysical characterization of explosive basaltic activity at Villarrica volcano: Journal of Geophysical Research: Solid Earth, v. 113, doi:10.1029/2007jb005328.

Hagemann, J.R. et al., 2024, A marine record of Patagonian ice sheet changes over the past 140,000 years: Proceedings of the National Academy of Sciences, v. 121, p. e2302983121, doi:10.1073/pnas.2302983121.

Harrison, S., Glasser, N., Winchester, V., Haresign, E., Warren, C., Duller, G.A.T., Bailey, R., Ivy-Ochs, S., Jansson, K., and Kubik, P., 2008, Glaciar León, Chilean Patagonia: late-Holocene chronology and geomorphology: The Holocene, v. 18, p. 643–652, doi:10.1177/0959683607086771.

Hein, A.S. et al., 2017, Regional mid-Pleistocene glaciation in central Patagonia: Quaternary Science Reviews, v. 164, p. 77–94, doi:10.1016/j.quascirev.2017.03.023.

Hickey -Vargas, R., Roa, H.M., Escobar, L.L., and Frey, F.A., 1989, Geochemical variations in Andean basaltic and silicic lavas from the Villarrica-Lanin volcanic chain (39.5°S): an evaluation of source heterogeneity, fractional crystallization and crustal assimilation: Contributions to Mineralogy and Petrology, v. 103, p. 361–386, doi:10.1007/BF00402922.

Hill, B.E., Leslie, B., and Connor, C.B., 1993, A review and analysis of dating techniques for Neogene and Quaternary volcanic rocks:

Hughes, M.K., and Diaz, H.F., 1994, Was there a medieval warm period?, and if so, where and when? Climatic Change, v. 26, p. 109–142, doi:10.1007/BF01092410.

Jara, C., Moreno, H., Mella, M., and Duhart, P., 2011, Geología del área Villarrica - Huiscapi, Regiones de La Araucanía y de Los Ríos:

Jomelli, V. et al., 2014, A major advance of tropical Andean glaciers during the Antarctic cold reversal: Nature, v. 513, p. 224–228, doi:10.1038/nature13546.

Kaplan, M.R. et al., 2016, Patagonian and southern South Atlantic view of Holocene climate: Quaternary Science Reviews, v. 141, p. 112–125, doi:10.1016/j.quascirev.2016.03.014.

Kaplan, M.R., Coronato, A., Hulton, N.R.J., Rabassa, J.O., Kubik, P.W., and Freeman, S.P.H.T., 2007, Cosmogenic nuclide measurements in southernmost South America and implications for landscape change: Geomorphology, v. 87, p. 284–301, doi:10.1016/j.geomorph.2006.10.005.

Kilian, R., and Lamy, F., 2012, A review of Glacial and Holocene paleoclimate records from southernmost Patagonia (49–55°S): Quaternary Science Reviews, v. 53, p. 1–23, doi:10.1016/j.quascirev.2012.07.017.

Knudson, K.P., Hendy, I.L., and Neil, H.L., 2011, Re-examining Southern Hemisphere westerly wind behavior: insights from a late Holocene precipitation reconstruction using New Zealand fjord sediments: Quaternary Science Reviews, v. 30, p. 3124–3138, doi:10.1016/j.quascirev.2011.07.017.

Koch, J., and Kilian, R., 2005, 'Little Ice Age' glacier fluctuations, Gran Campo Nevado, southernmost Chile: The Holocene, v. 15, p. 20–28, doi:10.1191/0959683605hl780rp.

Kurz, M.D., 1986, Cosmogenic helium in a terrestrial igneous rock: Nature, v. 320, p. 435–439, doi:10.1038/320435a0.

Kurz, M.D., Colodner, D., Trull, T.W., Moore, R.B., and O'Brien, K., 1990, Cosmic ray exposure dating with in situ produced cosmogenic 3He: Results from young Hawaiian lava flows: Earth and Planetary Science Letters, v. 97, p. 177–189, doi:10.1016/0012-821X(90)90107-9.

Lambeck, K., Rouby, H., Purcell, A., Sun, Y., and Sambridge, M., 2014, Sea level and global ice volumes from the Last Glacial Maximum to the Holocene: Proceedings of the National Academy of Sciences, v. 111, p. 15296–15303, doi:10.1073/pnas.1411762111.

Lamy, F., Kilian, R., Arz, H.W., Francois, J.-P., Kaiser, J., Prange, M., and Steinke, T., 2010, Holocene changes in the position and intensity of the southern westerly wind belt: Nature Geoscience, v. 3, p. 695–699, doi:10.1038/ngeo959.

Lamy, F., Prange, M., Arz, H.W., Varma, V., Kaiser, J., Kilian, R., Hefter, J., Benthien, A., and Mollenhauer, G., 2015, The Southern Westerlies During the Holocene: Paleoenvironmental Reconstructions from Chilean Lake, Fjord, and Ocean Margin Sediments Combined with Climate Modeling, *in* Schulz, M. and Paul, A. eds., Integrated Analysis of Interglacial Climate Dynamics (INTERDYNAMIC), Cham, Springer International Publishing, SpringerBriefs in Earth System Sciences, p. 75–81, doi:10.1007/978-3-319-00693-2_13.

Lara, L., and Clavero, J., 2004, Villarrica Volcano (39.5°S), Southern Andes, Chile:, https://www.researchgate.net/profile/Hugo-Roa-2/publication/284777198_Evolution_of_Villarrica_Volcano_IAVCEI_2004_Servicio_Nacional_de_Geologia_y_Mineria_Boletin_No_61_Luis_Lara_Jorge_Clavero_Editors/links/5b7c8dcba6fdcc5f8b5afe50/Evolution-of-Villarrica-Volcano-IAVCEI-2004-Servicio-

Nacional-de-Geologia-y-Mineria-Boletin-No-61-Luis-Lara-Jorge-Clavero-Editors.pdf?_sg%5B0%5D=started_experiment_milestone&origin=journalDetail&_rtd=e30%3D.

Laskar, J., Robutel, P., Joutel, F., Gastineau, M., Correia, A.C.M., and Levrard, B., 2004, A long-term numerical solution for the insolation quantities of the Earth: Astronomy & Astrophysics, v. 428, p. 261–285, doi:10.1051/0004-6361:20041335.

Leger, T.P.M., Hein, A.S., Bingham, R.G., Rodés, Á., Fabel, D., and Smedley, R.K., 2021, Geomorphology and 10Be chronology of the Last Glacial Maximum and deglaciation in northeastern Patagonia, 43°S-71°W: Quaternary Science Reviews, v. 272, p. 107194, doi:10.1016/j.quascirev.2021.107194.

Li, Y., Li, Y., Harbor, J., Liu, G., Yi, C., and Caffee, M.W., 2016, Cosmogenic 10Be constraints on Little Ice Age glacial advances in the eastern Tian Shan, China: Quaternary Science Reviews, v. 138, p. 105–118, doi:10.1016/j.quascirev.2016.02.023.

Lifton, N., Sato, T., and Dunai, T.J., 2014, Scaling in situ cosmogenic nuclide production rates using analytical approximations to atmospheric cosmic-ray fluxes: Earth and Planetary Science Letters, v. 386, p. 149–160, doi:10.1016/j.epsl.2013.10.052.

Lowell, T.V., Heusser, C.J., Andersen, B.G., Moreno, P.I., Hauser, A., Heusser, L.E., Schlüchter, C., Marchant, D.R., and Denton, G.H., 1995, Interhemispheric Correlation of Late Pleistocene Glacial Events: Science, v. 269, p. 1541–1549, doi:10.1126/science.269.5230.1541.

Luckman, B.H., 2000, The Little Ice Age in the Canadian Rockies: Geomorphology, v. 32, p. 357–384, doi:10.1016/S0169-555X(99)00104-X.

Malone, A.G.O., Pierrehumbert, R.T., Lowell, T.V., Kelly, M.A., and Stroup, J.S., 2015, Constraints on southern hemisphere tropical climate change during the Little Ice Age and Younger Dryas based on glacier modeling of the Quelccaya Ice Cap, Peru: Quaternary Science Reviews, v. 125, p. 106–116, doi:10.1016/j.quascirev.2015.08.001.

Mann, M.E., 2002, Little Ice Age, *in* Encyclopedia of global environmental change, v. 1, p. 504–509, chrome-extension://efaidnbmnnnibpcajpcglclefindmkaj/https://www.meteo.psu.edu/holocene/public_html/shared/articles/littleiceage.pdf.

Mann, M.E., Bradley, R.S., and Hughes, M.K., 1999, Northern hemisphere temperatures during the past millennium: Inferences, uncertainties, and limitations: Geophysical Research Letters, v. 26, p. 759–762, doi:10.1029/1999GL900070.

Mann, M.E., Zhang, Z., Rutherford, S., Bradley, R.S., Hughes, M.K., Shindell, D., Ammann, C., Faluvegi, G., and Ni, F., 2009, Global Signatures and Dynamical Origins of the Little Ice Age and Medieval Climate Anomaly: Science, v. 326, p. 1256–1260, doi:10.1126/science.1177303.

Marcott, S.A., Fountain, A.G., O'Connor, J.E., Sniffen, P.J., and Dethier, D.P., 2009, A latest Pleistocene and Holocene glacial history and paleoclimate reconstruction at Three Sisters and Broken Top Volcanoes, Oregon, U.S.A.: Quaternary Research, v. 71, p. 181–189, doi:10.1016/j.yqres.2008.09.002.

Marcott, S.A., Shakun, J.D., Clark, P.U., and Mix, A.C., 2013, A Reconstruction of Regional and Global Temperature for the Past 11,300 Years: Science, v. 339, p. 1198–1201, doi:10.1126/science.1228026.

Marta, S. et al., 2021, The Retreat of Mountain Glaciers since the Little Ice Age: A Spatially Explicit Database: Data, v. 6, p. 107, doi:10.3390/data6100107.

Masiokas, M.H. et al., 2020, A Review of the Current State and Recent Changes of the Andean Cryosphere: Frontiers in Earth Science, v. 8, p. 99, doi:10.3389/feart.2020.00099.

Masiokas, M.H., Luckman, B.H., Villalba, R., Delgado, S., Skvarca, P., and Ripalta, A., 2009, Little Ice Age fluctuations of small glaciers in the Monte Fitz Roy and Lago del Desierto areas, south Patagonian Andes, Argentina: Palaeogeography, Palaeoclimatology, Palaeoecology, v. 281, p. 351–362, doi:10.1016/j.palaeo.2007.10.031.

Matthews, J.A., and Briffa, K.R., 2005, The 'little ice age': re-evaluation of an evolving concept: Geografiska Annaler: Series A, Physical Geography, v. 87, p. 17–36, doi:10.1111/j.0435-3676.2005.00242.x.

Meier, W.J.-H., Grießinger, J., Hochreuther, P., and Braun, M.H., 2018, An Updated Multi-Temporal Glacier Inventory for the Patagonian Andes With Changes Between the Little Ice Age and 2016: Frontiers in Earth Science, v. 6, p. 62, doi:10.3389/feart.2018.00062.

Mendelová, M., Hein, A.S., Rodés, Á., Smedley, R.K., and Xu, S., 2020, Glacier expansion in central Patagonia during the Antarctic Cold Reversal followed by retreat and stabilisation during the Younger Dryas: Quaternary Science Reviews, v. 227, p. 106047, doi:10.1016/j.quascirev.2019.106047.

Meyer, I., and Wagner, S., 2009, The Little Ice Age in Southern South America: Proxy and Model Based Evidence, *in* Vimeux, F., Sylvestre, F., and Khodri, M. eds., Past Climate Variability in South America and Surrounding Regions, Dordrecht, Springer Netherlands, Developments in Paleoenvironmental Research, v. 14, p. 395–412, doi:10.1007/978-90-481-2672-9_16.

Miller, G.H. et al., 2012, Abrupt onset of the Little Ice Age triggered by volcanism and sustained by sea-ice/ocean feedbacks: Geophysical Research Letters, v. 39, p. 2011GL050168, doi:10.1029/2011GL050168.

Moreno, H., 2000, Mapa de peligros del volcán Villarrica, regiones de La Araucania y de Los Lagos:

Moreno, P.I. et al., 2018, Onset and Evolution of Southern Annular Mode-Like Changes at Centennial Timescale: Scientific Reports, v. 8, p. 3458, doi:10.1038/s41598-018-21836-6.

Moreno, H., and Clavero, J., 2006, Geología del Volcán Villarrica:

Moreno, P.I., Denton, G.H., Moreno, H., Lowell, T.V., Putnam, A.E., and Kaplan, M.R., 2015, Radiocarbon chronology of the last glacial maximum and its termination in northwestern Patagonia: Quaternary Science Reviews, v. 122, p. 233–249, doi:10.1016/j.quascirev.2015.05.027.

Moreno, P.I., Kaplan, M.R., François, J.P., Villa-Martínez, R., Moy, C.M., Stern, C.R., and Kubik, P.W., 2009, Renewed glacial activity during the Antarctic cold reversal and persistence of cold conditions until 11.5 ka in southwestern Patagonia: Geology, v. 37, p. 375–378, doi:10.1130/G25399A.1.

Moreno-Yaeger, P., Singer, B.S., Jicha, B.R., Edwards, B.R., Kurz, M.D., Mixon, E., Tremblay, M.M., Vera, F., and Fustos, I., unpublished, Magmatic evolution and glacial interplay of Villarrica (Rukapillán), the most active volcano in the Chilean Andes.:

Moy, C.M., Dunbar, R.B., Moreno, P.I., Francois, J.-P., Villa-Martínez, R., Mucciarone, D.M., Guilderson, T.P., and Garreaud, R.D., 2008, Isotopic evidence for hydrologic change related to the westerlies in SW Patagonia, Chile, during the last millennium: Quaternary Science Reviews, v. 27, p. 1335–1349, doi:10.1016/j.quascirev.2008.03.006.

Muñoz, M., 1983, Eruption patterns of the chilean volcanoes Villarrica, Llaima, and Tupungatito: pure and applied geophysics, v. 121, p. 835–852, doi:10.1007/bf02590184.

Nimick, D.A., McGrath, D., Mahan, S.A., Friesen, B.A., and Leidich, J., 2016, Latest Pleistocene and Holocene glacial events in the Colonia valley, Northern Patagonia Icefield, southern Chile: Journal of Quaternary Science, v. 31, p. 551–564, doi:10.1002/jqs.2847.

PAGES 2k Consortium, 2019, Consistent multidecadal variability in global temperature reconstructions and simulations over the Common Era: Nature Geoscience, v. 12, p. 643–649, doi:10.1038/s41561-019-0400-0.

PAGES 2k Consortium, 2013, Continental-scale temperature variability during the past two millennia: Nature Geoscience, v. 6, p. 339–346, doi:10.1038/ngeo1797.

PAGES2k Consortium et al., 2017, A global multiproxy database for temperature reconstructions of the Common Era: Scientific Data, v. 4, doi:10.1038/sdata.2017.88.

Pedro, J.B. et al., 2016, The spatial extent and dynamics of the Antarctic Cold Reversal: Nature Geoscience, v. 9, p. 51–55, doi:10.1038/ngeo2580.

Peltier, C., Kaplan, M.R., Sagredo, E.A., Moreno, P.I., Araos, J., Birkel, S.D., Villa-Martínez, R., Schwartz, R., Reynhout, S.A., and Schaefer, J.M., 2023, The last two glacial cycles in central Patagonia: A precise record from the Ñirehuao glacier lobe: Quaternary Science Reviews, v. 304, p. 107873, doi:10.1016/j.quascirev.2022.107873.

Petit-Breuilh Sepúlveda, M.E., 2006, La historia eruptiva de los volcanes hispanoamericanos (Siglos XVI al XX): El Modelo Chileno: Trébol Ediciones.

Porter, S.C., and Denton, G.H., 1967, Chronology of neoglaciation in the North American Cordillera: , p. 177–210.

Porter, P.R., Smart, M.J., and Irvine-Fynn, T.D.L., 2019, Glacial Sediment Stores and Their Reworking, *in* Heckmann, T. and Morche, D. eds., Geomorphology of Proglacial Systems, Cham, Springer International Publishing, Geography of the Physical Environment, p. 157–176, doi:10.1007/978-3-319-94184-4_10.

Price, B.N. et al., 2022, Chlorine-36 Surface Exposure Dating of Late Holocene Moraines and Glacial Mass Balance Modeling, Monte Sierra Nevada, South-Central Chilean Andes (38°S): Frontiers in Earth Science, v. 10, p. 848652, doi:10.3389/feart.2022.848652.

Putnam, A.E., Denton, G.H., Schaefer, J.M., Barrell, D.J.A., Andersen, B.G., Finkel, R.C., Schwartz, R., Doughty, A.M., Kaplan, M.R., and Schlüchter, C., 2010, Glacier advance in southern middle-latitudes during the Antarctic Cold Reversal: Nature Geoscience, v. 3, p. 700–704, doi:10.1038/ngeo962.

Putnam, A.E., Schaefer, J.M., Denton, G.H., Barrell, D.J.A., Birkel, S.D., Andersen, B.G., Kaplan, M.R., Finkel, R.C., Schwartz, R., and Doughty, A.M., 2013, The Last Glacial Maximum at 44°S documented by a 10Be moraine chronology at Lake Ohau, Southern Alps of New Zealand: Quaternary Science Reviews, v. 62, p. 114–141, doi:10.1016/j.quascirev.2012.10.034.

Rabassa, J., Coronato, A., Martínez, O., and Reato, A., 2022, Last Glacial Maximum, Late Glacial and Holocene of Patagonia, *in* Miotti, L., Salemme, M., and Hermo, D. eds., Archaeology of Piedra Museo Locality, Cham, Springer International Publishing, The Latin American Studies Book Series, p. 59–84, doi:10.1007/978-3-030-92503-1_2.

Reinthaler, J., Paul, F., Granados, H.D., Rivera, A., and Huggel, C., 2019, Area changes of glaciers on active volcanoes in Latin America between 1986 and 2015 observed from multi-temporal satellite imagery: Journal of Glaciology, v. 65, p. 542–556, doi:10.1017/jog.2019.30.

Renssen, H., Goosse, H., Roche, D.M., and Seppä, H., 2018, The global hydroclimate response during the Younger Dryas event: Quaternary Science Reviews, v. 193, p. 84–97, doi:10.1016/j.quascirev.2018.05.033.

Reynhout, S.A., Sagredo, E.A., Kaplan, M.R., Aravena, J.C., Martini, M.A., Moreno, P.I., Rojas, M., Schwartz, R., and Schaefer, J.M., 2019, Holocene glacier fluctuations in Patagonia are modulated by summer insolation intensity and paced by Southern Annular Mode-like variability: Quaternary Science Reviews, v. 220, p. 178–187, doi:10.1016/j.quascirev.2019.05.029.

Riechelson, H., Bova, S.C., Rosenthal, Y., Meyers, S., and Bu, K., 2023, Solar Cycles Forced Southern Westerly Wind Migrations During the Holocene: Geophysical Research Letters, v. 50, p. e2023GL104148, doi:10.1029/2023GL104148.

Rivera, A., Bown, F., Mella, R., Wendt, J., Casassa, G., Acuña, C., Rignot, E., Clavero, J., and Brock, B., 2006, Ice volumetric changes on active volcanoes in southern Chile: Annals of Glaciology, v. 43, p. 111–122, doi:10.3189/172756406781811970.

Rivera, A., Corripio, J.G., Brock, B., Clavero, J., and Wendt, J., 2008, Monitoring ice-capped active Volcán Villarrica, southern Chile, using terrestrial photography combined with automatic weather stations and global positioning systems: Journal of Glaciology, v. 54, p. 920–930, doi:10.3189/002214308787780076.

Rivera, A., Koppes, M., Bravo, C., and Aravena, J.C., 2012, Little Ice Age advance and retreat of Glaciar Jorge Montt, Chilean Patagonia: Climate of the Past, v. 8, p. 403–414, doi:10.5194/cp-8-403-2012.

Rivera, A., Koppes, M., Bravo, C., and Aravena, J.C., 2011, Little ice age advance and retreat of Glaciar Jorge Montt, Chilean Patagonia, recorded in maps, air photographs and dendrochronology:, doi:10.5194/cpd-7-3131-2011.

Roe, G.H., Christian, J.E., and Marzeion, B., 2021, On the attribution of industrial-era glacier mass loss to anthropogenic climate change: The Cryosphere, v. 15, p. 1889–1905, doi:10.5194/tc-15-1889-2021.

Rowan, A.V., 2017, The 'Little Ice Age' in the Himalaya: A review of glacier advance driven by Northern Hemisphere temperature change: The Holocene, v. 27, p. 292–308, doi:10.1177/0959683616658530.

Russell, J.L., Dixon, K.W., Gnanadesikan, A., Stouffer, R.J., and Toggweiler, J.R., 2006, The Southern Hemisphere Westerlies in a Warming World: Propping Open the Door to the Deep Ocean: Journal of Climate, v. 19, p. 6382–6390, doi:10.1175/jcli3984.1.

Sagredo, E.A., Kaplan, M.R., Araya, P.S., Lowell, T.V., Aravena, J.C., Moreno, P.I., Kelly, M.A., and Schaefer, J.M., 2018, Trans-pacific glacial response to the Antarctic Cold Reversal in the southern mid-latitudes: Quaternary Science Reviews, v. 188, p. 160–166, doi:10.1016/j.quascirev.2018.01.011.

Sagredo, E.A., Lowell, T.V., Kelly, M.A., Rupper, S., Aravena, J.C., Ward, D.J., and Malone, A.G., 2016, Equilibrium line altitudes along the Andes during the Last millennium: Paleoclimatic implications: The Holocene, v. 27, p. 1019–1033, doi:10.1177/0959683616678458.

Schaefer, J.M. et al., 2009, High-Frequency Holocene Glacier Fluctuations in New Zealand Differ from the Northern Signature: Science, v. 324, p. 622–625, doi:10.1126/science.1169312.

Schmittner, A., Yoshimori, M., and Weaver, A.J., 2002, Instability of Glacial Climate in a Model of the Ocean- Atmosphere-Cryosphere System: Science, v. 295, p. 1489–1493, doi:10.1126/science.1066174.

Scott, W.E., 1977, Quaternary glaciation and volcanism, Metolius River area, Oregon: Geological Society of America Bulletin, v. 88, p. 113, doi:10.1130/0016-7606(1977)88<113:qgavmr>2.0.co;2.

Shakun, J.D., Clark, P.U., He, F., Marcott, S.A., Mix, A.C., Liu, Z., Otto-Bliesner, B., Schmittner, A., and Bard, E., 2012, Global warming preceded by increasing carbon dioxide concentrations during the last deglaciation: Nature, v. 484, p. 49–54, doi:10.1038/nature10915.

Sigl, M. et al., 2015, Timing and climate forcing of volcanic eruptions for the past 2,500 years: Nature, v. 523, p. 543–549, doi:10.1038/nature14565.

Simms, A.R., Bentley, M.J., Simkins, L.M., Zurbuchen, J., Reynolds, L.C., DeWitt, R., and Thomas, E.R., 2021, Evidence for a “Little Ice Age” glacial advance within the Antarctic Peninsula – Examples from glacially-overrun raised beaches: Quaternary Science Reviews, v. 271, p. 107195, doi:10.1016/j.quascirev.2021.107195.

Solomina, O.N. et al., 2016, Glacier fluctuations during the past 2000 years: Quaternary Science Reviews, v. 149, p. 61–90, doi:10.1016/j.quascirev.2016.04.008.

Solomina, O.N. et al., 2015, Holocene glacier fluctuations: Quaternary Science Reviews, v. 111, p. 9–34, doi:10.1016/j.quascirev.2014.11.018.

Steinhilber, F., Beer, J., and Fröhlich, C., 2009, Total solar irradiance during the Holocene: Geophysical Research Letters, v. 36, p. 2009GL040142, doi:10.1029/2009GL040142.

Stocker, T.F., 1998, The Seesaw Effect: Science, v. 282, p. 61–62, doi:10.1126/science.282.5386.61.

Stocker, T.F., and Johnsen, S.J., 2003, A minimum thermodynamic model for the bipolar seesaw: Paleoceanography, v. 18, p. 2003PA000920, doi:10.1029/2003PA000920.

Strelin, J.A., Kaplan, M.R., Vandergoes, M.J., Denton, G.H., and Schaefer, J.M., 2014, Holocene glacier history of the Lago Argentino basin, Southern Patagonian Icefield: Quaternary Science Reviews, v. 101, p. 124–145, doi:10.1016/j.quascirev.2014.06.026.

Thouret, J.C., Ramírez C., J., Gibert-Malengreau, B., Vargas, C.A., Naranjo, J.L., Vandemeulebrouck, J., Valla, F., and Funk, M., 2007, Volcano–glacier interactions on composite cones and lahar generation: Nevado del Ruiz, Colombia, case study: Annals of Glaciology, v. 45, p. 115–127, doi:10.3189/172756407782282589.

Törnqvist, T.E., and Hijma, M.P., 2012, Links between early Holocene ice-sheet decay, sea-level rise and abrupt climate change: Nature Geoscience, v. 5, p. 601–606, doi:10.1038/ngeo1536.

Turney, C.S.M. et al., 2016, Multidecadal variations in Southern Hemisphere atmospheric ^{14}C: Evidence against a Southern Ocean sink at the end of the Little Ice Age CO_2 anomaly: Global Biogeochemical Cycles, v. 30, p. 211–218, doi:10.1002/2015GB005257.

Van Daele, M. et al., 2014, The 600 yr eruptive history of Villarrica Volcano (Chile) revealed by annually laminated lake sediments: Geological Society of America Bulletin, v. 126, p. 481–498, doi:10.1130/b30798.1.

Vandergoes, M.J., Newnham, R.M., Preusser, F., Hendy, C.H., Lowell, T.V., Fitzsimons, S.J., Hogg, A.G., Kasper, H.U., and Schlüchter, C., 2005, Regional insolation forcing of late Quaternary climate change in the Southern Hemisphere: Nature, v. 436, p. 242–245, doi:10.1038/nature03826.

Varma, V., Prange, M., Lamy, F., Merkel, U., and Schulz, M., 2011, Solar-forced shifts of the Southern Hemisphere Westerlies during the Holocene: Climate of the Past, v. 7, p. 339–347, doi:10.5194/cp-7-339-2011.

Varma, V., Prange, M., Spangehl, T., Lamy, F., Cubasch, U., and Schulz, M., 2012, Impact of solar-induced stratospheric ozone decline on Southern Hemisphere westerlies during the Late Maunder Minimum: Geophysical Research Letters, v. 39, p. 2012GL053403, doi:10.1029/2012GL053403.

Villalba, R., 1994, Tree-ring and glacial evidence for the medieval warm epoch and the little ice age in southern South America: Climatic Change, v. 26, p. 183–197, doi:10.1007/BF01092413.

Voigt, I., Chiessi, C.M., Prange, M., Mulitza, S., Groeneveld, J., Varma, V., and Henrich, R., 2015, Holocene shifts of the southern westerlies across the South Atlantic: Paleoceanography, v. 30, p. 39–51, doi:10.1002/2014PA002677.

Wanner, H. et al., 2008, Mid- to Late Holocene climate change: an overview: Quaternary Science Reviews, v. 27, p. 1791–1828, doi:10.1016/j.quascirev.2008.06.013.

Wanner, H., Mercolli, L., Grosjean, M., and Ritz, S.P., 2015, Holocene climate variability and change; a data-based review: Journal of the Geological Society, v. 172, p. 254–263, doi:10.1144/jgs2013-101.

Wanner, H., Pfister, C., and Neukom, R., 2022, The variable European Little Ice Age: Quaternary Science Reviews, v. 287, p. 107531, doi:10.1016/j.quascirev.2022.107531.

Wanner, H., Solomina, O., Grosjean, M., Ritz, S.P., and Jetel, M., 2011, Structure and origin of Holocene cold events: Quaternary Science Reviews, v. 30, p. 3109–3123, doi:10.1016/j.quascirev.2011.07.010.

Weber, M.E., Kuhn, G., Sprenk, D., Rolf, C., Ohlwein, C., and Ricken, W., 2012, Dust transport from Patagonia to Antarctica – A new stratigraphic approach from the Scotia Sea and its implications for the last glacial cycle: Quaternary Science Reviews, v. 36, p. 177–188, doi:10.1016/j.quascirev.2012.01.016.

Winkler, S., 2000, The 'Little Ice Age' maximum in the Southern Alps, New Zealand: preliminary results at Mueller Glacier: The Holocene, v. 10, p. 643–647, doi:10.1191/095968300666087656.

Zhang, W., Wu, H., Cheng, J., Geng, J., Li, Q., Sun, Y., Yu, Y., Lu, H., and Guo, Z., 2022, Holocene seasonal temperature evolution and spatial variability over the Northern Hemisphere landmass: Nature Communications, v. 13, p. 5334, doi:10.1038/s41467-022-33107-0.

Figures and Tables

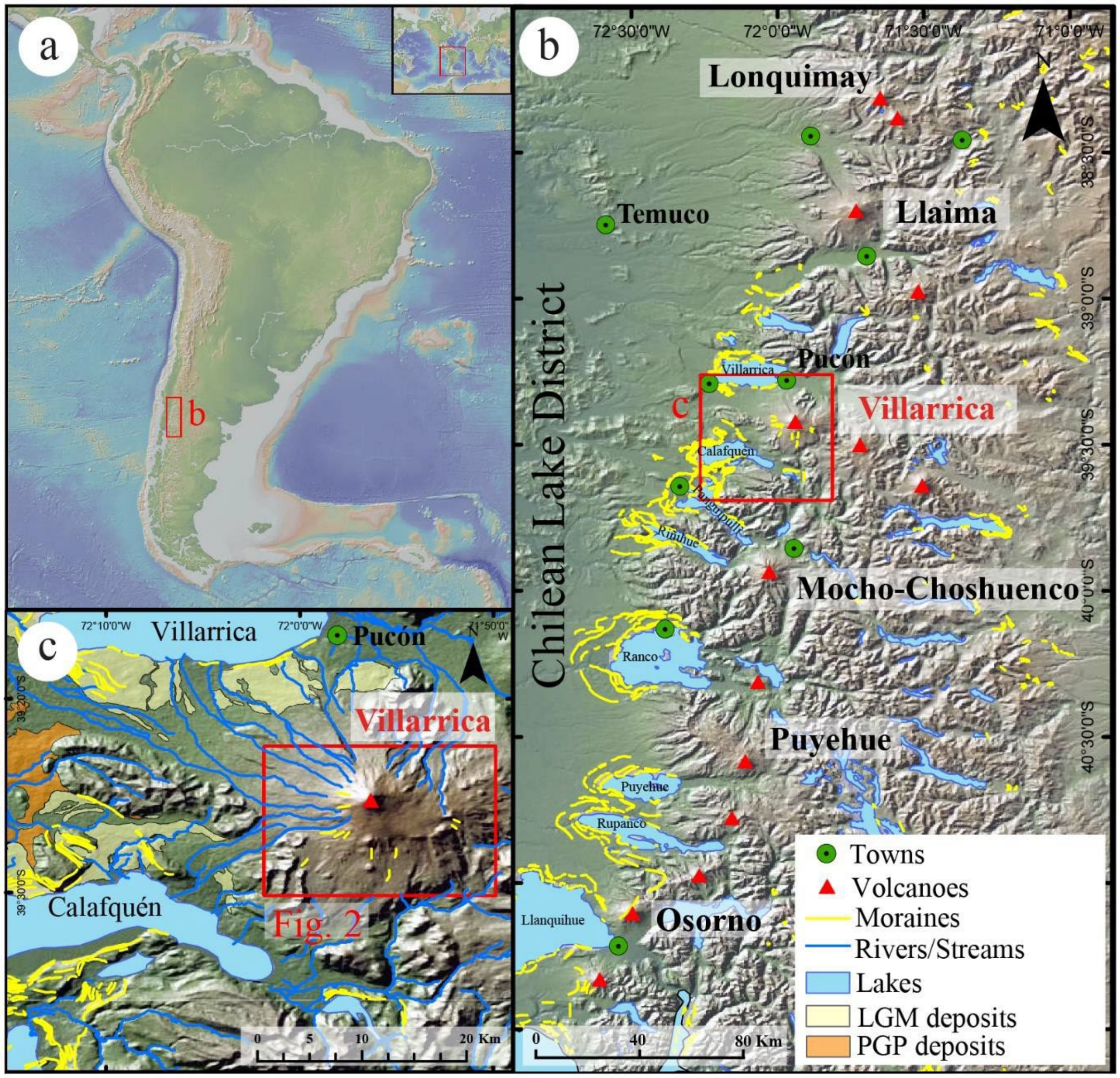

Figure 1. Setting of the present research in South America (a) within the Chilean Lake District (b) and the Araucanía Region (c). The yellow line represents moraine ridges, while light-yellow polygons show the Last Glacial Maximum (LGM) deposits and orange polygons illustrate the Penultimate Glacial Period (PGP) deposits. The Southern Volcanic Zone is represented by red triangles where volcanoes are located. Adapted from Davies et al. (2020).

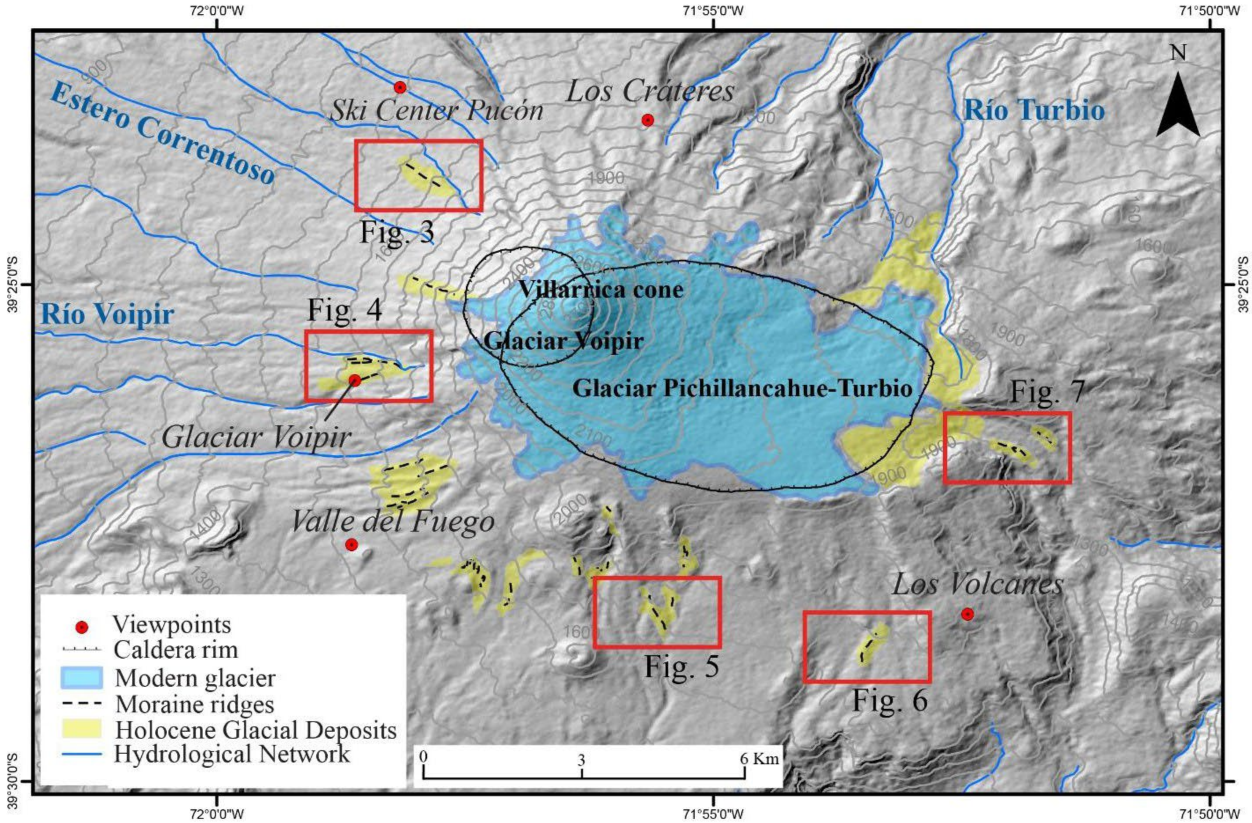

Figure 2. Villarrica volcano surface features. Present-day glaciers are shown in light blue, Holocene glacial landforms in yellow, and moraine ridges as black dashed-lines. Note that Villarrica has two caldera rims, with Glaciar Pichillancahue-Turbio located within the larger of the two. Red boxes denote the locations of Figures 3-7, which are western, southern, and eastern sample collection locations.

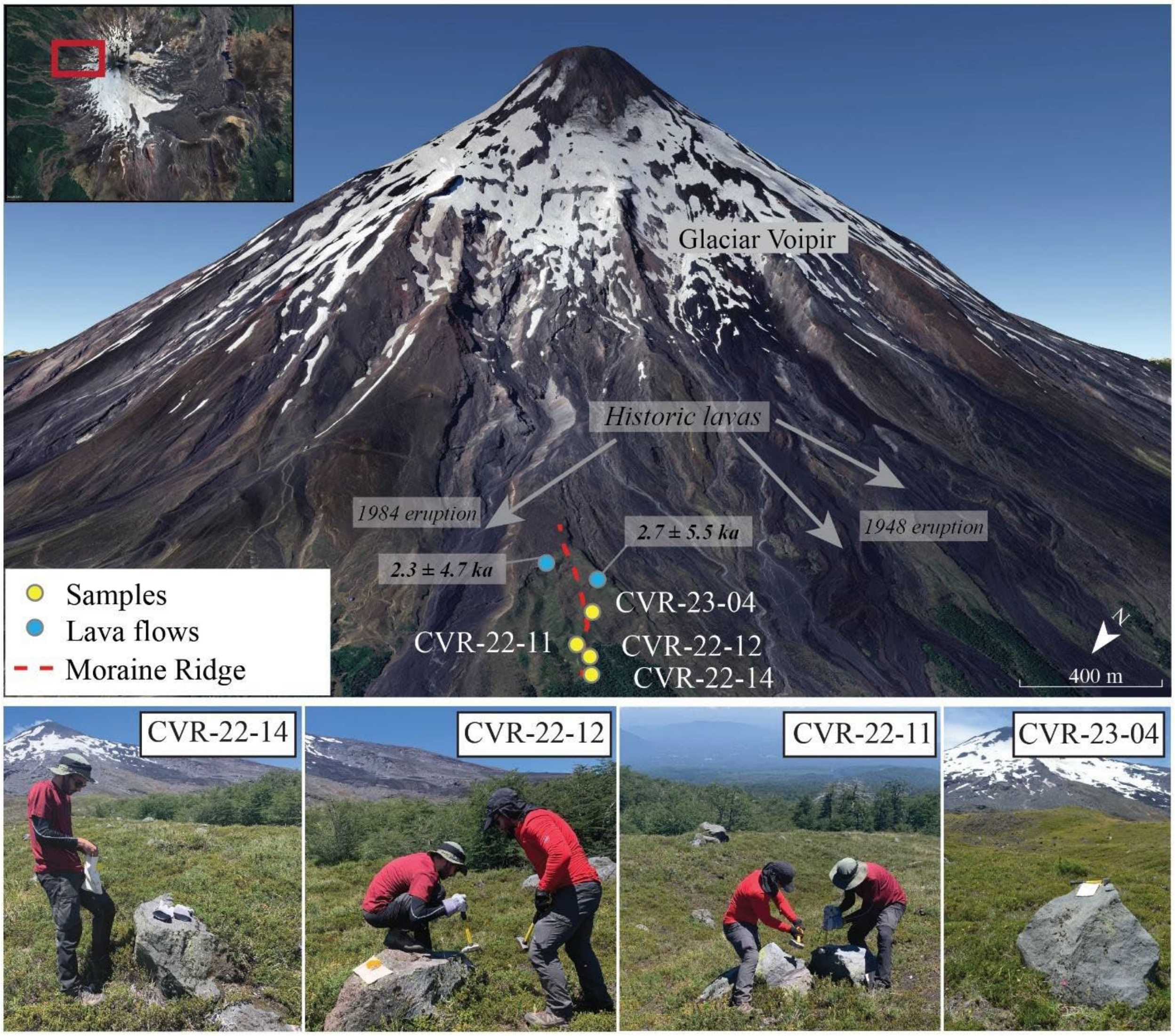

Figure 3. Northwestern moraine ridges with selected boulder sampling sites. Field photographs show the erratic boulders that were sampled and analyzed for this work. A late Holocene lava flow underlies this moraine (Moreno-Yaeger et al, unpublished), while it is encircled by historic lava flows from 1948 and 1984 eruptions, delineating its boundaries and providing a contextual framework for understanding the timing of glacial and volcanic events. Modified CNES/Airbus imagery taken from Google Earth Pro.

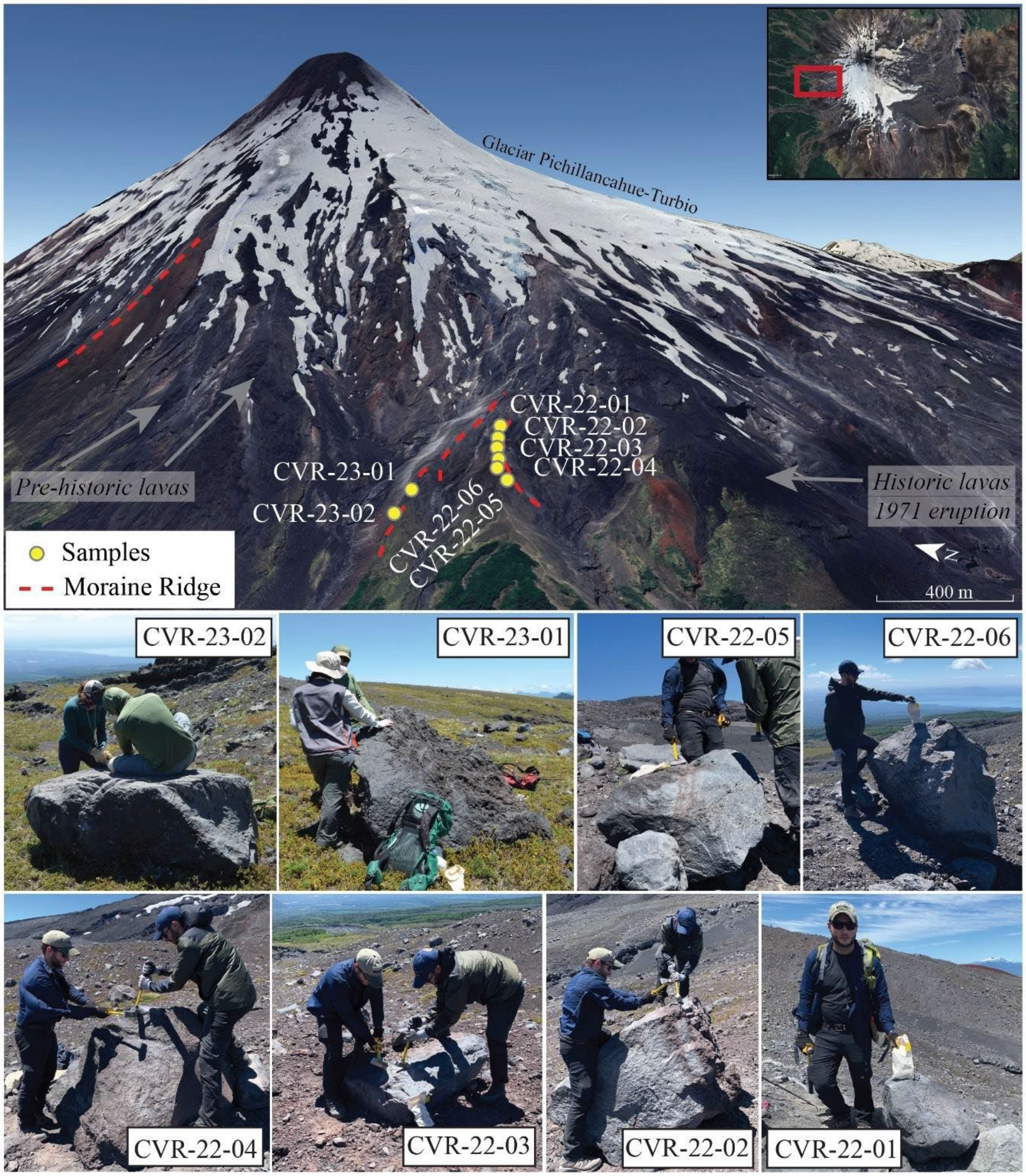

Figure 4. Western moraine ridges with selected boulder sampling sites. Field photographs show the erratic boulders that were sampled and analyzed for this work. Pre-historic and historic lava flows from the 1971 eruption are observed encircling the moraine. Modified CNES/Airbus imagery taken from Google Earth Pro.

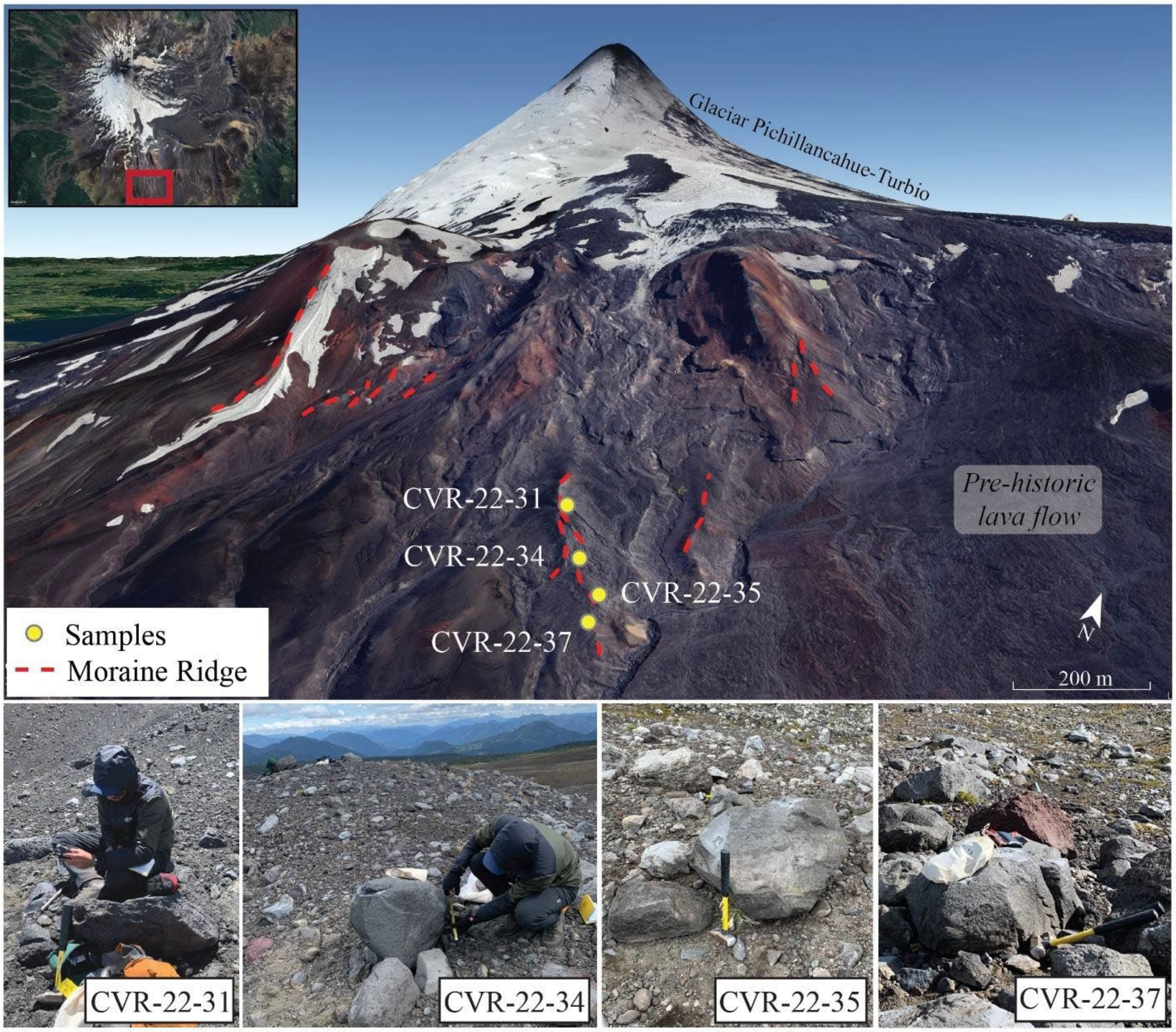

Figure 5. Southern moraine ridges with selected boulder sampling sites. Field photographs show the erratic boulders that were sampled and analyzed for this work. Pre-historic lava flows are observed in the figure. Modified CNES/Airbus imagery taken from Google Earth Pro.

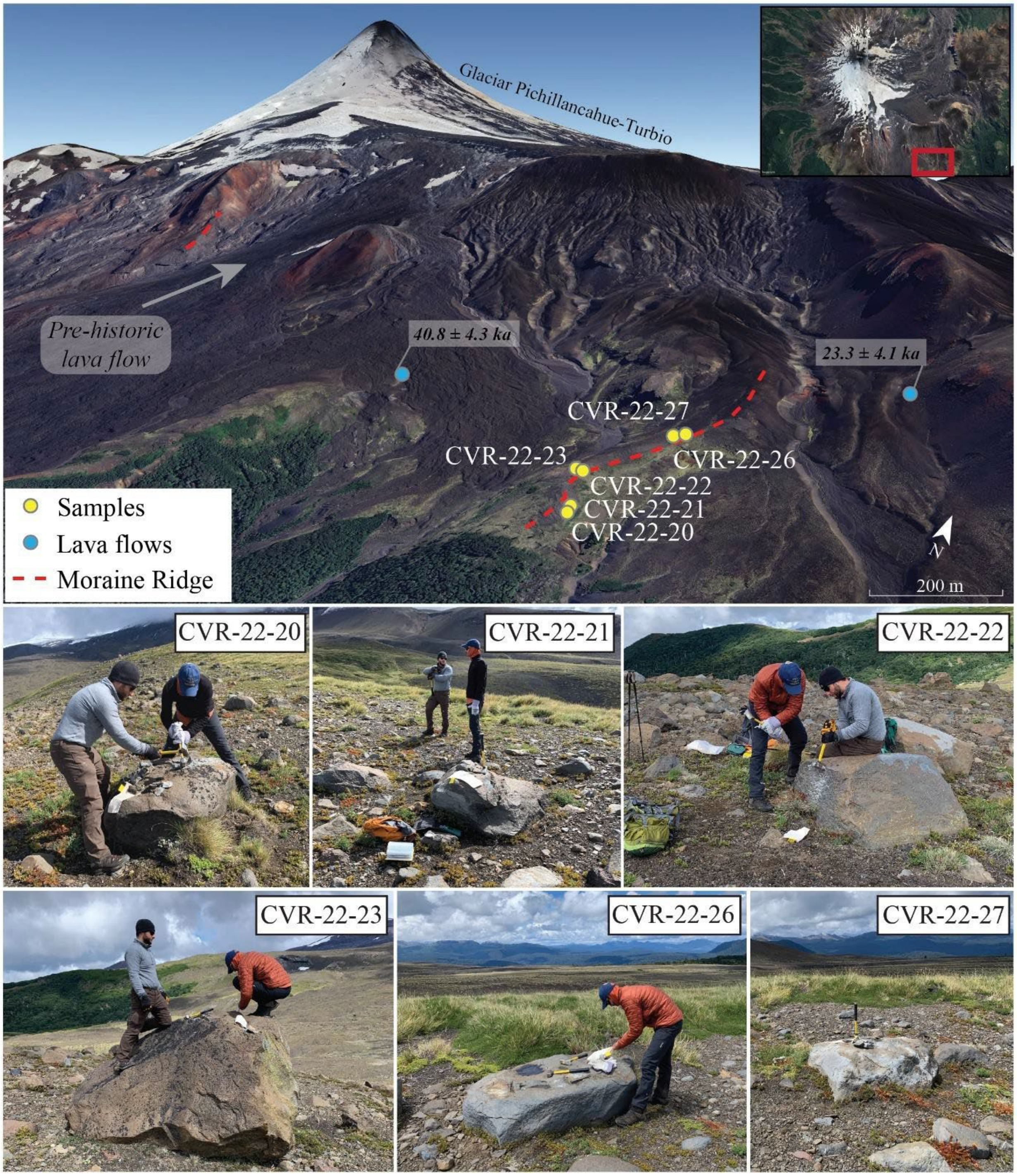

Figure 6. Southeastern moraine ridges with selected boulder sampling sites. Field photographs show the erratic boulders that were sampled and analyzed for this work. The moraine is encircled by Late Pleistocene lava flows (Moreno-Yaeger et al., unpublished). Modified CNES/Airbus imagery taken from Google Earth Pro.

Figure 7. Eastern moraine ridges with selected boulder sampling sites. Field photographs show the erratic boulders that were sampled and analyzed for this work. A pre-historic lava flow is observed between the mapped moraine ridges. Modified CNES/Airbus imagery taken from Google Earth Pro.

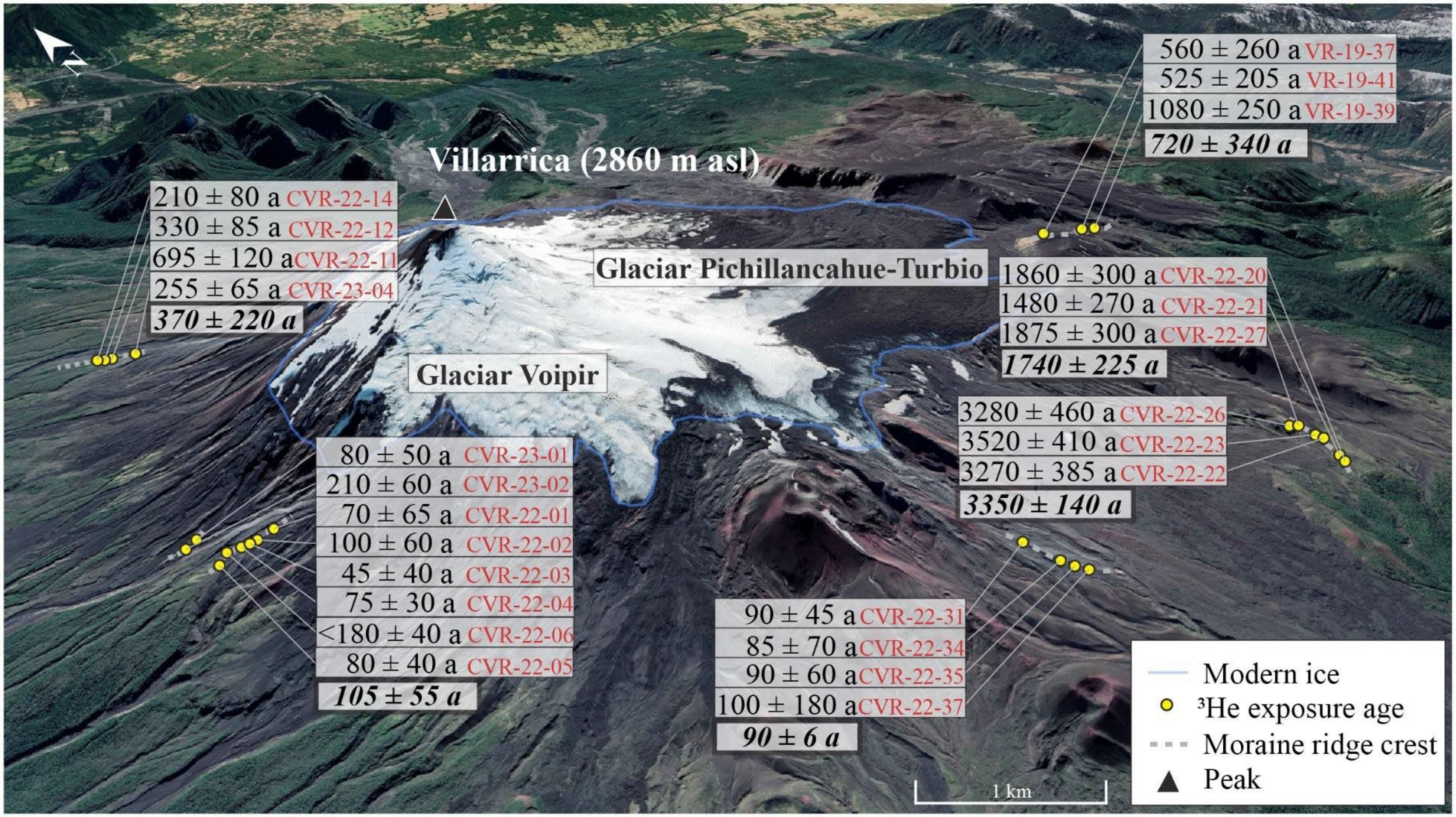

Figure 8. Cosmogenic ^{3}He exposure ages of moraine boulders at Villarrica volcano. Mean ages with standard deviations are also shown for each moraine. A dashed grey line indicates moraine ridge crests, and a blue line delimits modern ice. Glaciar Pichillancahue-Turbio is partially covered by debris-ash. Modified CNES/Airbus imagery taken from Google Earth Pro.

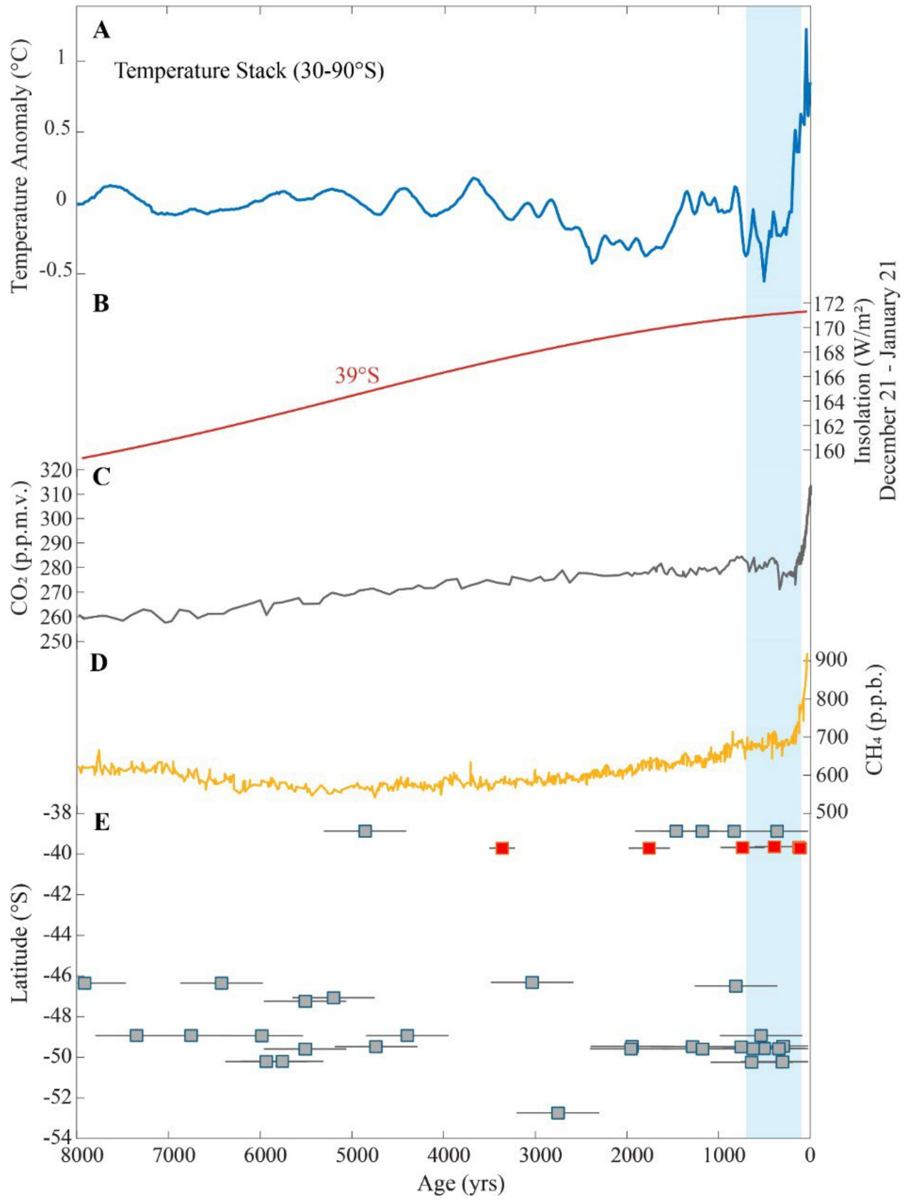

Figure 9. Temporal variations in climate and glacial activity in Patagonia. The figure displays A) the Anomaly of zonal mean temperature reconstruction (temperature stack) along 30-90°S (Marcott et al., 2013); B) the insolation curve for the Southern Hemisphere (39°S latitude) alongside records of atmospheric CO_2 (B) and CH_4 (C) concentrations (Bereiter et al., 2015; Beck et al., 2018; respectively). At the bottom (E), a compilation of cosmogenic mean ages with associated standard deviations is presented indicating glacial advancements (Douglass et al., 2005; Kaplan et al., 2007, 2016; Harrison et al., 2008; Strelin et al., 2014; Sagredo et al., 2016; Nimick et al., 2016; Hein et al., 2017; Reynhout et al., 2019; Price et al., 2022). The shaded polygon highlights the temporal extent of the LIA.

Table 1. Locational and geometric data for all cosmogenic samples for this research.

Sample	Rock type	Lat (°)	Lon (°)	Elevation (m asl)	Boulder Height (cm)	Sample Thickness (cm)	Topographic Shielding Correction Factor
VR-19-37	Basaltic andesite	-39.4433	-71.8687	1636	135	2.00	0.9903
VR-19-39	Basaltic andesite	-39.4445	-71.8651	1629	55	3.00	0.9880
VR-19-41	Basaltic andesite	-39.4448	-71.8648	1624	30	4.50	0.9903
CVR-22-01	Basaltic andesite	-39.4296	-71.7939	1572	65	2.75	0.9943
CVR-22-02	Basaltic andesite	-39.4314	-71.9724	1592	110	3.00	0.9943
CVR-22-03	Basaltic andesite	-39.4314	-71.9728	1577	35	3.00	0.9943
CVR-22-04	Basaltic andesite	-39.4315	-71.9732	1582	86	2.75	0.9854
CVR-22-05	Basaltic andesite	-39.4317	-71.9737	1569	69	2.00	0.9943
CVR-22-06	Basaltic andesite	-39.4314	-71.9736	1571	122	3.00	0.9882
CVR-22-11	Basaltic andesite	-39.3970	-71.9673	1394	38	3.00	0.9954
CVR-22-12	Basaltic andesite	-39.3969	-71.9676	1393	90	2.75	0.9954
CVR-22-14	Basaltic andesite	-39.3968	-71.9678	1390	70	3.25	0.9716
CVR-23-04	Basaltic andesite	-39.3978	-71.9666	1415	95	3.00	0.9871
CVR-22-20	Basaltic andesite	-39.4797	-71.8913	1463	57	2.75	0.9989
CVR-22-21	Basaltic andesite	-39.4796	-71.8913	1462	90	3.00	0.9982
CVR-22-22	Basaltic andesite	-39.4783	-71.8917	1475	50	2.50	0.9974
CVR-22-23	Basaltic andesite	-39.4783	-71.8919	1475	187	3.50	0.9989
CVR-22-26	Basaltic andesite	-39.4766	-71.8904	1467	50	2.25	0.9989
CVR-22-27	Basaltic andesite	-39.4767	-71.8905	1474	48	3.25	0.9989
CVR-22-31	Basaltic	-39.4704	-71.9269	1586	42	4.00	0.9984
CVR-22-34	Basaltic andesite	-39.4725	-71.9258	1530	47	4.50	0.9984
CVR-22-35	Basaltic andesite	-39.4731	-71.9252	1525	43	3.00	0.9984
CVR-22-37	Basaltic andesite	-39.4736	-71.9251	1515	47	3.50	0.9939
CVR-23-01	Basaltic andesite	-39.4292	-71.9761	1513	107	2.50	0.9972
CVR-23-02	Basaltic andesite	-39.4291	-71.9767	1504	65	3.00	0.9964

Table 2. Helium measurement data for all samples. When the He concentration cannot be resolved above the background (i.e. at the detection limit), it is defined as ''bdl''.

Sample	Olivine mass (g) Crushing	Olivine mass (g) Heating	$^{3}He_{tot}$ ($\times 10^{5}$ atoms)	$^{4}He_{tot}$ ($\times 10^{9}$ atoms)	R/Ra_{crush}	LSDn (1σ) Age (yrs) ± Ext (yrs)
VR-19-37	0.4131	0.4020	0.75 ± 0.3	0.79 ± 0.03	9.1060	558 ± 261
VR-19-39	0.7784	0.6017	1.47 ± 0.3	0.70 ± 0.03	5.3051	1080 ± 253
VR-19-41	0.7440	0.3877	0.62 ± 0.2	0.81 ± 0.03	4.9116	525 ± 205
CVR-22-01	0.9226	0.7921	0.29 ± 0.11	4.86 ± 0.20	3.3961	73 ± 67
CVR-22-02	0.8307	0.5123	0.22 ± 0.09	2.85 ± 0.04	2.7873	98 ± 58
CVR-22-03	1.0537	0.8100	0.16 ± 0.09	2.49 ± 0.05	3.2866	43 ± 42
CVR-22-04	0.9323	1.3670	0.34 ± 0.10	2.97 ± 0.05	3.5730	75 ± 29
CVR-22-05	0.9032	0.8867	0.24 ± 0.09	1.85 ± 0.03	1.9320	81 ± 40
CVR-22-06	1.2227	0.9937	0.23 ± 0.09	7.15 ± 0.11	2.4958	181 ± 42
CVR-22-11	1.0474	0.6581	1.22 ± 0.15	3.04 ± 0.06	2.2032	694 ± 118
CVR-22-12	0.8756	0.6995	0.64 ± 0.12	4.40 ± 0.07	1.3948	329 ± 85
CVR-22-14	0.9655	0.6737	0.53 ± 0.12	8.33 ± 0.29	1.9574	212 ± 85
CVR-23-04	1.2701	0.7163	0.51 ± 0.09	3.88 ± 0.06	2.3465	253 ± 64
CVR-22-20	0.9776	0.5138	2.99 ± 0.34	2.13 ± 0.05	2.4862	1858 ± 297
CVR-22-21	0.9920	0.4653	2.18 ± 0.30	2.50 ± 0.05	bdl	1479 ± 268
CVR-22-22	0.9560	0.9354	9.09 ± 0.39	4.06 ± 0.07	bdl	3267 ± 386
CVR-22-23	0.8531	0.9823	10.16 ± 0.39	6.27 ± 0.14	bdl	3517 ± 411
CVR-22-26	0.9572	0.4806	4.65 ± 0.41	1.52 ± 0.04	1.6133	3276 ± 462
CVR-22-27	0.8916	0.5239	3.09 ± 0.34	2.87 ± 0.06	0.5154	1874 ± 296
CVR-22-31	1.0176	1.0377	0.33 ± 0.12	3.76 ± 0.06	2.5295	87 ± 45
CVR-22-34	0.7596	0.7185	0.21 ± 0.12	2.01 ± 0.04	bdl	86 ± 68
CVR-22-35	0.8879	0.8703	0.27 ± 0.12	2.79 ± 0.07	bdl	92 ± 57
CVR-22-37	0.8161	1.0904	0.41 ± 0.13	42.03 ± 0.94	0.2464	99 ± 179
CVR-23-01	0.9940	1.0283	0.34 ± 0.13	5.15 ± 0.12	1.9268	79 ± 51
CVR-23-02	0.9178	0.9919	0.59 ± 0.14	3.12 ± 0.07	1.9456	209 ± 61

Table 3. Cosmogenic ^3He data with aliquots labeled alphabetically (e.g. a,b,c) indicating the number of aliquots analyzed per sample. It includes corrected and uncorrected values, as well as the corrected weighted mean for each sample.

Moraine	Sample	Aliquot	$^3He_{cosm}$ corrected, individual R_{crush} (atoms/g)	± (1σ)	$^3He_{cosm}$ corrected, weighted mean R_{crush} (atoms/g)	± (1σ)	$^3He_{cosm}$ uncorrected (atoms/g)	± (1σ)
Eastern	VR-19-37	bc	161892.1	73628.6	-	-	185875.3	73246.1
	VR-19-39	ab	265876.8	60031.9	-	-	278248.8	59799.6
	VR-19-39	cd	457891.2	88944.3	-	-	470551.4	88820.9
	VR-19-41	ab	152546.5	56896.9	-	-	167289.5	56682.5
	VR-19-41	cd	140435.9	53344.8	-	-	153241.3	53172.2
Western	CVR-22-01	abc	11567.8	45772.1	16404.4	25643.5	27609.6	25283.9
	CVR-22-01	defghi	13796.8	13827.0	21619.3	8793.6	39741.8	8705.8
	CVR-22-02	abc	bdl	bdl	bdl	bdl	bdl	bdl
	CVR-22-02	defg	16880.6	18698.0	25678.3	14942.4	38463.5	14917.3
	CVR-22-03	bcdef	4649.7	13727.0	11353.3	11051.0	19379.1	11037.4
	CVR-22-04	abcdefgh	19582.9	8993.8	19539.5	7146.8	25208.4	7136.4
	CVR-22-05	abcde	–	–	21096.0	10139.6	26532.4	10132.8
	CVR-22-06	efghij	bdl	bdl	4634.3	9430.3	23416.4	9344.4
	CVR-23-01	abcdef	19365.0	14455.2	19791.2	12538.7	32866.7	12505.6
	CVR-23-02	abcdef	51101.8	14095.0	51281.0	13927.2	59495.9	13915.4
North-western	CVR-22-11	abcd	171550.0	22830.4	173137.7	22438.9	185195.0	22423.6
	CVR-22-12	abcd	79553.3	17685.2	74901.3	17567.7	91305.0	17532.5
	CVR-22-14	abcd	46183.2	18070.9	46437.6	17802.2	78220.2	17672.4
	CVR-23-04	abcd	54416.2	13097.4	57545.3	12971.1	71691.6	12935.7
Southeastern	CVR-22-20	abc	568412.6	66602.8	571771.0	66331.1	582607.0	66326.9
	CVR-22-21	abc	–	–	454276.7	65229.8	468310.7	65222.6
	CVR-22-22	abcdef	–	–	960458.0	41211.2	971767.9	41204.1
	CVR-22-23	abcdef	–	–	1017573.6	40040.0	1034232.1	40023.2
	CVR-22-26	abc	961262.5	85548.2	959849.3	84628.5	968098.1	84626.5
	CVR-22-27	abc	590455.6	67336.5	580018.3	65935.2	594213.9	65928.1
Southern	CVR-22-31	abcdef	19933.4	12004.6	22765.7	11580.9	32229.8	11563.2
	CVR-22-34	abcd	–	–	21473.6	16792.3	28783.8	16784.9
	CVR-22-35	abcde	–	–	23163.8	14102.2	31529.3	14089.8
	CVR-22-37	abcdef	24549.1	44014.7	bdl	bdl	37277.5	11510.9

Appendices

A: Probability Density Function of Moraine Ages

Here we present the probability density functions (PDFs) for cosmogenic ^{3}He exposure ages of boulders from the moraines on various flanks of Villarrica volcano. Each subfigure (A-E) corresponds to individual moraines, and subfigure (F) shows the combined PDF for all the moraines.

Among the datasets, the southeastern moraine (C) exhibits a distinct bimodal distribution, which likely reflects two separate glacial advances. This bimodal set of ages suggests that the glacier advanced, deposited boulders, retreated, and then advanced again, depositing additional boulders without significantly disturbing the earlier deposits. This supports the hypothesis that two distinct glacial events contributed to the moraine formation at this location.

In contrast, Panels A and B show apparent bimodal peaks. However, they are unrelated to true bimodal age distribution as they likely represent outliers within our dataset rather than distinct glacial events. Due to the limited number of samples, we have chosen to retain these outliers for the sake of data completeness. Importantly, removing these outliers would not significantly alter the overall age of the moraine or the interpretation of the glaciation events (Appendix B). Moreover, Panels D and E primarily indicate different periods of glacial advances rather than multiple separate glaciations like the southeastern moraine.

The combined PDF (F) integrates the exposure ages from all moraines, reflecting the complex glacial history of Villarrica volcano, where both the timing of glaciations and the interaction between glacial and volcanic processes contributed to moraine formation.

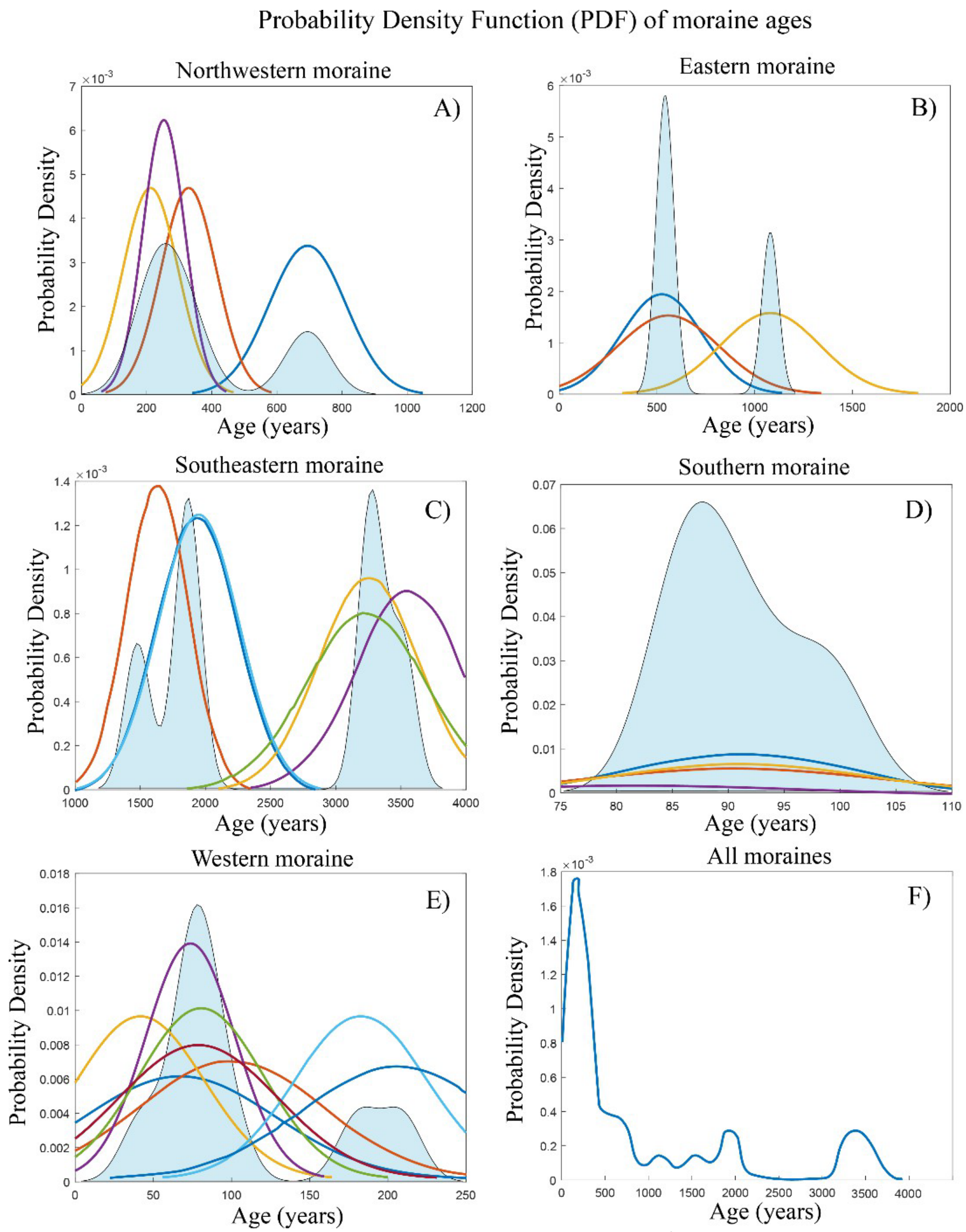

Figure A1. Probability density functions (PDFs) for cosmogenic ^{3}He exposure ages from boulders on the moraines of Villarrica volcano. Panels A-E correspond to individual moraines with their boulder ages, while Panel F shows the combined PDF. The southeastern moraine (C) displays a distinct bimodal distribution, indicating two separate glacial advances. In contrast, while apparent bimodal peaks are observed in A and B, these are likely to represent outliers rather than true separate glacial events, and D and E show different periods of glacial advances rather than multiple separate glaciations. The combined PDF (F) reflects the complex glacial history of Villarrica volcano, shaped by both glaciations and volcanic processes.

B: Overlapping PDFs for LIA moraines

This appendix includes a figure comparing the probability density functions (PDFs) for the cosmogenic ^3He exposure ages of boulders (represented by mean ages and standard deviation) from the Little Ice Age (LIA) moraines on the northwestern and eastern flanks of Villarrica volcano. The figure shows two sets of overlapping PDFs: one that includes outliers (left panel) and one that excludes them (right panel).

- Left Panel (with outliers): The overlap area, shaded in green, indicates the shared range of ages between the two moraines. Including the outliers' results in a wider age distribution for both moraines, particularly broadening the tails of the PDFs, which contributes to the variability in age estimates.
- Right Panel (without outliers): When the outliers are excluded, the PDFs for both moraines become narrower, with sharper peaks and a slightly more defined overlap area. The general pattern remains similar, suggesting that removing outliers does not significantly alter the age overlap between the two moraines. The overlap area is almost unchanged, despite the reduced uncertainty in the distributions.

Given our limited dataset for these moraines, we decided to retain the outliers in the analysis. The overlap between the moraines' age distributions remains consistent regardless of whether the outliers are included or not, supporting the conclusion that their inclusion does not drastically affect the interpretation of the overall glaciation events.

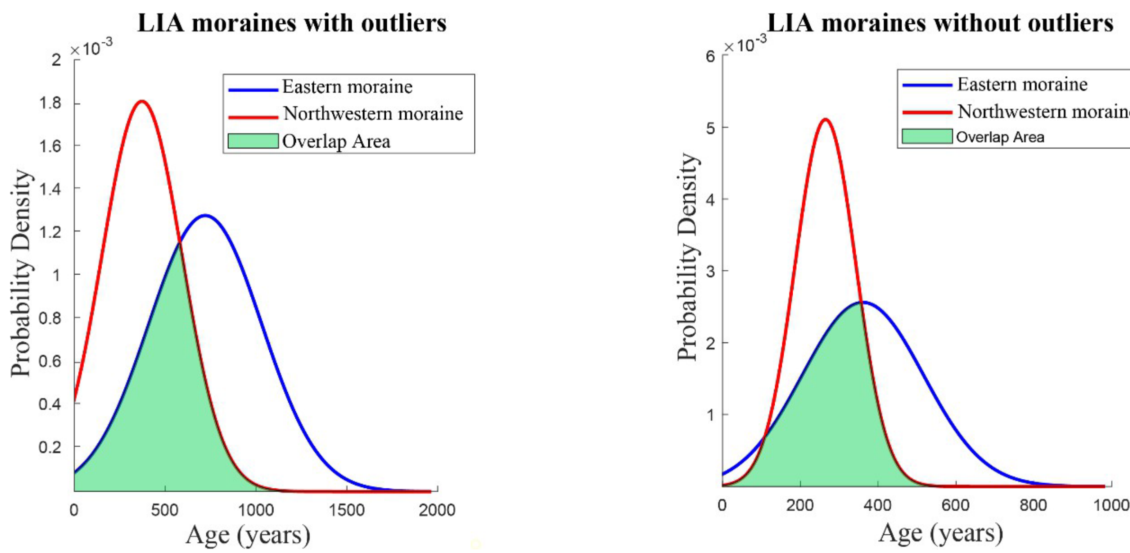

Figure A2. Comparison of PDFs for cosmogenic ^{3}He exposure ages of boulders from the LIA moraines on the northwestern and eastern flanks of Villarrica volcano. The left panel includes outliers, with the overlap area shaded in green, showing a wider age distribution due to the outliers. The right panel excludes outliers, resulting in narrower PDFs with sharper peaks, though the overlap area remains largely unchanged. Despite reduced uncertainty when outliers are excluded, their inclusion does not significantly affect the interpretation of the moraine age overlap or the glaciation events.

C: Formation of the bimodal age distribution

This appendix provides a schematic representation of the processes that formed the bimodal age distribution observed in the southeastern moraine at Villarrica volcano. The series of panels (A-F) in the figure illustrates the sequence of glacial advances and retreats, interacting with preexisting lava flows (green colors), and how these dynamics deposited boulders during two distinct phases.

- Panel A: The glacier begins to advance into the valley, slowly moving toward the lava flow.
- Panel B: The glacier continues advancing until it reaches the height of the preexisting lava flow. At this point, the glacier has nearly filled the valley.
- Panel C: As the glacier retreats, it deposits the first set of boulders directly onto the surface of the lava flow. These boulders represent the initial glacial advance and are the older population in the bimodal age distribution.
- Panel D: The glacier advances again, reaching approximately the same height as the lava flow during this second phase of glaciation.

- Panel E: The second retreat deposits a new set of boulders in the same area without significantly disturbing the previously deposited ones. This results in the bimodal age distribution, where two distinct populations of boulders are preserved.
- Panel F: Post-glacial processes, such as erosion or fluvial activity, may slightly modify the landscape but do not significantly disturb the boulders. The two distinct phases of deposition remain intact, preserving the bimodal distribution of ages.

This sequence explains how the interaction between the glacier and the lava flow led to the bimodal age distribution observed in the moraine. The two separate phases of glacier advance and retreat deposited boulders at similar heights but during different periods, resulting in the distinct age populations reflected in the probability density function (PDF) for this moraine (Appendix A, c).

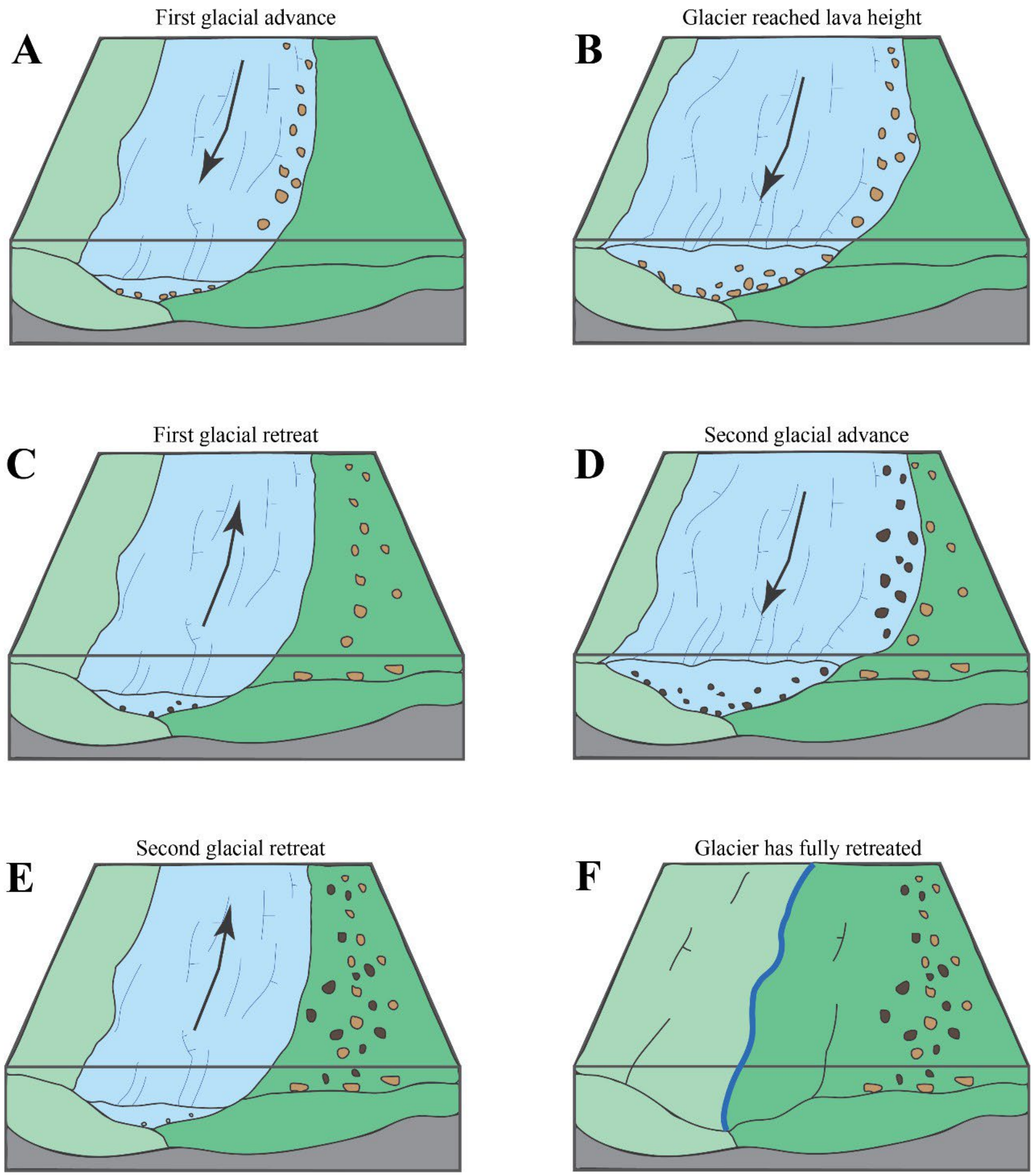

Figure A3. Schematic representation of the processes that formed the bimodal age distribution in the southeastern moraine at Villarrica volcano. Panels A-F illustrate the sequence of glacial advances and retreats interacting with preexisting lava flows (green). Panel A: Glacier begins advancing into the valley. Panel B: Glacier reaches the height of the lava flow. Panel C: First retreat deposits older boulders onto the lava flow. Panel D: The second advance reaches similar heights. Panel E: The second retreat deposits younger boulders without disturbing the older ones, creating the bimodal age distribution. Panel F: Post-glacial processes slightly modify the landscape while preserving the bimodal age pattern.